The Astronomical Journal, 166:110 (16pp), 2023 September https://doi.org/10.3847/1538-3881/ace76c
© 2023. The Author(s). Published by the American Astronomical Society.
OPEN ACCESS

Binary Star Evolution in Different Environments: Filamentary, Fractal, Halo, and Tidal Tail Clusters

Xiaoying Pang[1,2], Yifan Wang[1], Shih-Yun Tang[3,4], Yicheng Rui[5,6], Jing Bai[1], Chengyuan Li[7,8], Fabo Feng[5,6], M. B. N. Kouwenhoven[1], Wen-Ping Chen[9], and Rwei-ju Chuang[10]

[1] Department of Physics, Xi'an Jiaotong-Liverpool University, 111 Ren'ai Road, Dushu Lake Science and Education Innovation District, Suzhou 215123, Jiangsu Province, People's Republic of China; Xiaoying.Pang@xjtlu.edu.cn
[2] Shanghai Key Laboratory for Astrophysics, Shanghai Normal University, 100 Guilin Road, Shanghai 200234, People's Republic of China
[3] Lowell Observatory, 1400 West Mars Hill Road, Flagstaff, AZ 86001, USA
[4] Department of Physics and Astronomy, Rice University, 6100 Main Street, Houston, TX 77005, USA
[5] Tsung-Dao Lee Institute, Shanghai Jiao Tong University, Shengrong Road 520, Shanghai 201210, People's Republic Of China
[6] School of Physics and Astronomy, Shanghai Jiao Tong University, 800 Dongchuan Road, Shanghai 200240, People's Republic of China
[7] School of Physics and Astronomy, Sun Yat-sen University, Daxue Road, Zhuhai 519082, People's Republic of China
[8] CSST Science Center for the Guangdong-Hong Kong-Macau Greater Bay Area, Zhuhai 519082, People's Republic of China
[9] Institute of Astronomy, National Central University, 300 Zhongda Road, Zhongli, Taoyuan 32001, Taiwan
[10] Fu-Jen Catholic University, Institute of Applied Statistics, 510 Zhongzheng Road, Xinzhuang Dist, New Taipei City 24205, Taiwan
Received 2023 May 7; revised 2023 July 11; accepted 2023 July 12; published 2023 August 17

Abstract

Using membership of 85 open clusters from previous studies based on Gaia Data Release 3 data, we identify binary candidates in the color–magnitude diagram for systems with mass ratio $q > 0.4$. The binary fraction is corrected for incompleteness at different distances due to the Gaia angular resolution limit. We find a decreasing binary fraction with increasing cluster age, with substantial scatter. For clusters with a total mass $>200\ M_\odot$, the binary fraction is independent of cluster mass. The binary fraction depends strongly on stellar density. Among the four types of cluster environments, the lowest-density filamentary and fractal stellar groups have the highest mean binary fraction: 23.6% and 23.2%, respectively. The mean binary fraction in tidal tail clusters is 20.8% and is lowest in the densest halo-type clusters: 14.8%. We find clear evidence of early disruptions of binary stars in the cluster sample. The radial binary fraction depends strongly on the clustercentric distance across all four types of environments, with the smallest binary fraction within the half-mass radius r_h and increasing toward a few r_h. Only hints of mass segregation are found in the target clusters. The observed amounts of mass segregation are not significant enough to generate a global effect inside the target clusters. We evaluate the bias of unresolved binary systems (assuming a primary mass of $1\ M_\odot$) in 1D tangential velocity, which is 0.1–1 km s^{-1}. Further studies are required to characterize the internal star cluster kinematics using Gaia proper motions.

Unified Astronomy Thesaurus concepts: Open star clusters (1160); Star clusters (1567); Binary stars (154); Dynamical evolution (421)

1. Introduction

Binary systems play a critical role in our understanding of the star formation process. The likelihood of a star being in a binary system is positively correlated with the mass of the star (Raghavan et al. 2010; Sana et al. 2012; Duchêne & Kraus 2013; Offner et al. 2022). Binary stars can originate from either the fragmentation of protostellar cores, filaments, or accretion disks or from dynamical interactions between stars (Moeckel & Bally 2007; Bate 2012; Moe et al. 2019; Offner et al. 2022). The properties of binary stars exhibit significant variations, depending on the specific conditions under which the star formation process occurs. To understand the conditions leading to different binary populations, it is therefore necessary to investigate the frequency of the observed binaries across clustered environments of different density and morphology—ranging from dispersing filamentary stellar groups or associations and disrupted tidal tail clusters to dense spherical halo-type star clusters (e.g., Pang et al. 2022b)—to gain a better understanding of the star formation process.

Original content from this work may be used under the terms of the Creative Commons Attribution 4.0 licence. Any further distribution of this work must maintain attribution to the author(s) and the title of the work, journal citation and DOI.

Low-density stellar groups, such as associations, have a wide binary fraction similar to the field star population (e.g., Kouwenhoven et al. 2005, 2007; Reipurth et al. 2007; Kraus et al. 2011). However, the binary fraction in dense open clusters, such as the Pleiades, the Praesepe cluster, and Alpha Per, falls below that of the field (Deacon & Kraus 2020). In such dense clustered environments, primordial wide binary systems are efficiently disrupted by stellar encounters and are unable to survive until they become members of the field (e.g., Kroupa 2001; Portegies Zwart et al. 2001; Reipurth et al. 2007; Parker et al. 2009). The survival probability of a binary system depends on the binding energy of the system, the strengths of the encounters, and the frequency of such encounters (Reipurth et al. 2014). In low-mass, loosely bound clusters, a greater proportion of binary systems can survive the destruction process, due to the lower encounter rate and the smaller mean kinetic energy of the colliding stars (Sollima et al. 2010).

According to the hierarchical formation scenario postulated by Kruijssen (2012), regions of high stellar density are the birthplaces of dense, bound clusters. In contrast, loose filamentary groups of stars are frequently formed in environments with lower stellar densities (Pang et al. 2022b). The observed binaries in the Galactic field result from a combination of relatively unprocessed binaries from loose stellar groups

and highly processed binaries from dense clusters. Consequently, wide stellar binaries in the field are more likely to have originated from loose stellar groups, while close/intermediate binaries can originate from either source.

The density of the stellar environment plays a significant role in the evolution of binary systems. A correlation between the binary fraction and cluster density has been observed in globular clusters, with higher-density environments having lower binary fractions than their lower-density counterparts (Sollima et al. 2007). A similar correlation has been observed between the binary fraction and the cluster's integrated absolute magnitude, with brighter clusters having a smaller binary fraction. Brighter clusters have a higher number of stellar members and their stellar densities are generally higher. The rate at which close encounters occur is expected to be higher in massive clusters, which causes the disruption of a large fraction of primordial binary systems (Milone et al. 2008). However, this trend is not always evident in open clusters, particularly those younger than 100 Myr (Jaehnig et al. 2017; Kounkel et al. 2019).

Besides stellar density, the age of a cluster has a significant impact on the spatial distribution of binary systems. When the cluster dynamically ages, the process of two-body relaxation leads to mass segregation, causing an increase in the binary fraction toward the center of globular clusters (Sollima et al. 2007; Milone et al. 2012). This trend has also been found in *N*-body simulations (Portegies Zwart et al. 2004; Shu et al. 2021). As a consequence of mass segregation, most massive binaries migrate to the cluster center. This process is accelerated when a young, substructured cluster experiences mergers (e.g., Allison et al. 2009). Strong and frequent encounters in the center can cause binaries to harden and can in some cases result in Roche-lobe overflow or coalescence, leading to the formation of blue stragglers and cataclysmic variable stars (Hurley et al. 2001; Pang et al. 2022a). Sollima et al. (2007) find that in 13 low-density globular clusters, there is a clear negative correlation between binary fraction and age, suggesting that longer processing times increase the likelihood of binary destruction. However, when the sample is expanded to 59 clusters in Milone et al. (2012), there is no clear evidence to support such a correlation.

Open clusters are much younger than globular clusters and they are therefore expected to have a higher binary fraction on average. However, no clear dependence of the binary fraction on cluster age was found in the five open clusters studied by Sollima et al. (2010), which may be attributed to the limited sample size. Many studies have been conducted to examine the binary fraction within individual open clusters (Cohen et al. 2019; Jerabkova et al. 2019; Li et al. 2020; Jadhav et al. 2021; Malofeeva et al. 2022, 2023). However, there are numerous examples in the literature where the measured binary fractions obtained for the same open cluster are different. These inconsistencies in the published properties of the binary population for the same cluster may be attributed to differences in cluster member identification and binary selection methods. To elucidate the relationship between binary fraction, age, and stellar density, a uniform analysis of a large sample of open clusters covering a wide range of ages and masses is required. Young open clusters are particularly useful for investigating the primordial binary content and the process of binary disruption in the early stages of cluster evolution. We will use a consistent reduction approach to identify the binary content for 85 open clusters whose members have been determined via the same approach in Pang et al. (2021a, 2021b, 2022b) and Li et al. (2021). By averaging the uniform binary data, we aim to obtain a comprehensive overview of binary evolution in different clustered environments.

This paper is organized as follows. In Section 2, the data and membership are introduced. In Section 3, we present the binary identification and the related uncertainties. We correct the binary fraction for incompleteness and derive the total binary fraction given different mass ratio profiles. We then discuss the dependence of the binary fraction on the cluster parameters in Section 4. In Section 5, we investigate the evolution of the binary population in different clustered environments (i.e., different morphological types). The radial distributions of the binary systems in the representative clusters are presented in Section 5.2. In Section 5.3, we present how mass segregation affects the representative clusters among the four morphological types, and we study its relation to binarity. In Section 6, the 1D velocity dispersion of the clusters is measured, with simulations to estimate the binaries' effect on the measured dispersion. We crossmatch our results to previous studies in Section 7. Finally, we provide a brief summary of our findings in Section 8.

2. Gaia Data and Cluster Membership

In this study, we utilize member stars from a sample of 85 open clusters, as identified in previous works by Pang et al. (2021a, 2021b, 2022b) and Li et al. (2021). Note that these four studies required member stars to have parallaxes and photometric measurements within 10% uncertainties. When the binary component separation is close to the Gaia resolution limit, binary stars will suffer from worse astrometric solutions than single stars. Hence these unresolved binary systems may be removed in the aforementioned studies. The estimate of the unresolved binary systems in this work will be a lower limit, due to this bias. However, it is a common disadvantage for present-day investigations. The selection of members is performed with the aid of the machine-learning algorithm `StarGo` (Yuan et al. 2018), which makes use of the Gaia Early Data Release 3 (EDR3) data (Gaia Collaboration et al. 2021). The member stars are selected with a contamination rate of 5% (first developed in Pang et al. 2020), resulting in a corresponding membership probability of 95%.

All stars present in Gaia EDR3, with solutions, should be treated as single stars, with no other sources within the minimum angular resolution. The photometry used in this study is based on two-parameter solutions. For neighboring sources that are distinctly separate and have an angular separation of $0\farcs18$–$0\farcs6$, only two-parameter solutions were available (Lindegren et al. 2021). In Figure 6 of Lindegren et al. (2021), the angular separation for sources with a G magnitude of 15 mag is about $0\farcs6$. In this study, we treat $0\farcs6$ as the minimum angular resolution for Gaia data, beyond which a single star can be distinguished. Any stars with neighbors closer than $0\farcs6$ are deemed unresolved binaries.

Following the correction of G-band photometry in Gaia DR3 by Riello et al. (2021), the uncertainty in the photometry of sources with magnitudes fainter than $G = 13$ mag has been improved. In order to obtain more accurate photometric and kinematic data for each star, we crossmatch the members of these 85 clusters with Gaia DR3 (Gaia Collaboration et al. 2022). Our analysis subsequently relies on the data from Gaia DR3.

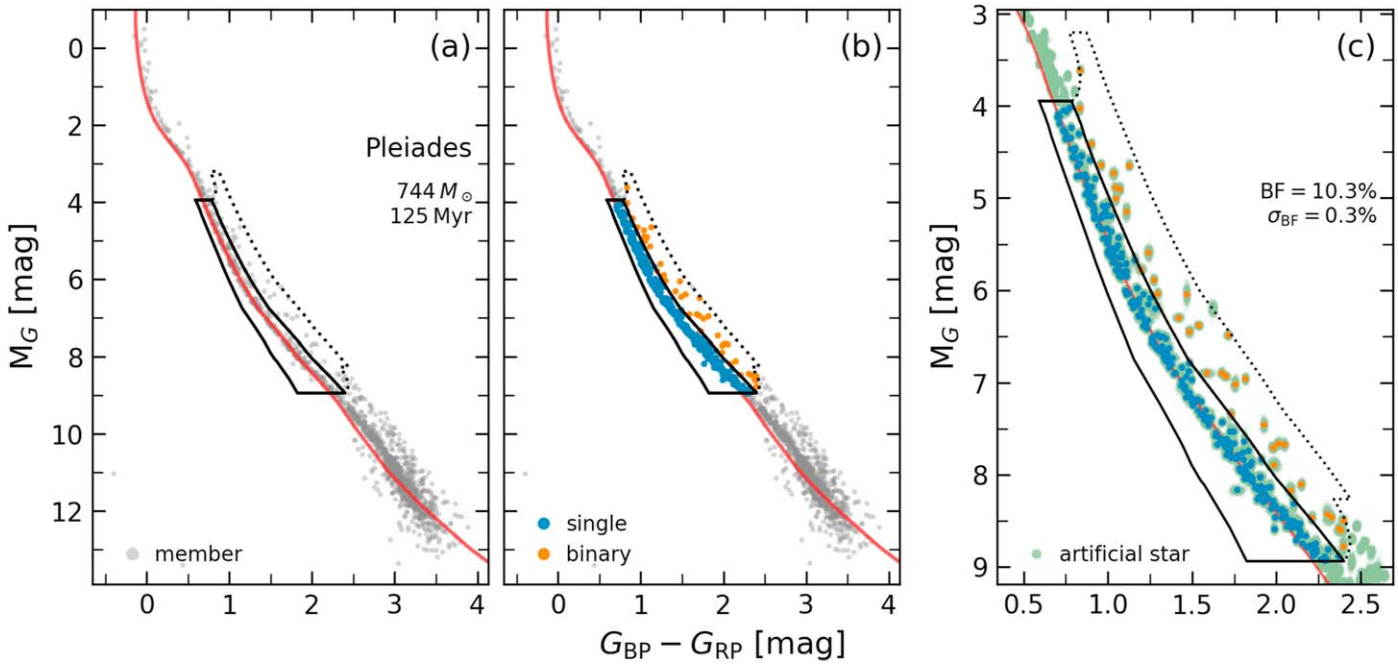

Figure 1. Binary identification via the CMD. The Pleiades cluster is shown as an example. (a) Best-fitted isochrone for the Pleiades (red curve). The region enclosed by the solid curve demarcates the single-star boundary defined in this work, whereas the dotted curve identifies the binary region. The right boundary of the solid polygon is the binary isochrone of $q = 0.4$, which is the boundary that we use to separate single and binary stars. The upper limit of the solid boundary is $M_G = 4$ mag and the lower limit is $0.5M_\odot$ ($M_G = 9 - 10$ mag). Members of the Pleiades are overplotted (gray circles). (b) Stars within the solid curve boundary are selected as single stars and are highlighted as blue dots. Binary stars (orange dots) are stars located within the binary boundary (dashed curves). (c) A zoom-in on the binary selection region. The green dots in the background are artificial stars produced via Monte Carlo simulations based on the photometric uncertainty (see the error estimation in Section 3.2 for details).

3. Binary Identification

3.1. Binary Selection through the Color–Magnitude Diagram

Unresolved binary systems with different mass ratios exhibit distinct features in the color–magnitude diagram (CMD). Through this study, we define the mass ratio as $q = M_2/M_1$, where M_1 is the mass of the primary star and M_2 is the mass of the secondary star ($M_2 \leqslant M_1$). Unresolved binary systems appear redder and brighter than the main sequence (MS) in the CMD. When the binary components are of equal mass $q = 1$, they form a distinctive "binary sequence" that is parallel to the MS and is 0.75 mag brighter. Unresolved binaries with high q (i.e., $q > 0.7$) are located at a significant distance from the MS ridgeline and are therefore relatively easy to detect. On the other hand, binaries with small q are located near the MS ridgeline, making them difficult to distinguish from single MS stars.

To select binary candidates, we identify stars located on the red side of the MS ridgeline. In this study, we adopt the best-fitted PARSEC isochrones (Bressan et al. 2012; Chen et al. 2015) from Pang et al. (2021a, 2021b, 2022b) and Li et al. (2021) to represent the MS ridgeline, since they also provide information about stellar masses and cluster age. The stellar mass will be used to determine the binary–single boundary, and the cluster age is a key parameter in the binary correlation investigation (see Section 4.3). Moreover, the deviation of the best-fit isochrone from the cluster ridgeline occurs mainly for the faint stars (e.g., M dwarfs), which are below our binary selection region (the solid and dotted polygons in Figure 1) and therefore will not affect the binary identification in this work. The systematic error for all clusters from isochrone fitting is identical, so the investigated relations of all clusters, e.g., the binary fraction and other variables, will not be influenced by the choice of the isochrone. Considering the negligible shifts of unresolved binaries with small q from the MS ridgeline, we only study binary systems with $q > q_0$, where q_0 is a certain minimum, so we can identify binary cluster members with high confidence. To accomplish this, we adopt the approach from Milone et al. (2012) and identify unresolved binary stars with higher-mass ratios $q > 0.4$ (see Figure 1).

We set the binary isochrone of $q_0 = 0.4$ as the boundary between single and binary stars (the right boundary of the solid polygon in Figure 1). We compute the binary isochrone by treating the two components in the binary system as unresolved. Any stars at locations that are both brighter and redder than this binary isochrone ($q_0 = 0.4$) are considered as unresolved binary stars or multiple systems. Throughout this study, we do not consider the possibility of triple systems or higher-order multiples. The difference between the best-fitted single isochrone and the binary isochrone of $q_0 = 0.4$ is considered as the typical width of the single region. On the left side of the best-fitting isochrone, we establish the left boundary of the single-star region as three to five times the typical width, depending on the photometric uncertainty. To establish the upper limit of the binary region, we adopt the fiducial binary isochrone for $q = 1$, which is 0.75 mag brighter than the single-star isochrone. Additionally, we add a photometric uncertainty of 0.1 mag to the $q = 1$ binary isochrone, to be the right boundary of the binary region.

When a pre-MS (PMS) star rotates fast (Li et al. 2017, 2019; Cordoni et al. 2018), it will appear redder than the MS stars and resemble an unresolved binary system. Cordoni et al. (2018)

have shown that nearly all star clusters exhibit a substantial amount of MS broadening due to rotating MS stars with an absolute G magnitude of less than 4 mag. The latest study by He et al. (2022) suggests that binary systems with a mass ratio of less than 0.6 are indistinguishable from rapidly rotating stars based on their colors. On the other hand, circumstellar disks around PMS stars, such as young class II objects, can make them appear redder compared to the diskless class III objects. These young stellar objects have a typical spectral type of M1 (e.g., López-Valdivia et al. 2021), where the effective temperature is estimated to range from roughly 3600 K (Pecaut & Mamajek 2013) to 3700 K (Herczeg & Hillenbrand 2014). According to the PMS evolutionary track by Baraffe et al. (2015), at the age of 3 Myr (our youngest cluster), an effective temperature 3600–3700 K corresponds to a stellar mass of 0.5–0.7 solar masses. Therefore, to avoid contamination due to accretion disks and fast rotation, we limit the selection of single and binary stars to those with a stellar mass greater than 0.5 $M_\odot$ (corresponding to $M_G = 9$–10 mag in clusters of different ages) and an absolute G magnitude fainter than $M_G = 4$ mag (the upper and lower boundaries of both the single and the binary boundary, i.e., the regions outlined by the solid and dotted curves in Figures 1(a), (b), and (c)).

The binary candidates are therefore mainly FGK stars. Any observed members outside the two regions described above are considered outliers and are excluded when calculating the binary fraction. Figure 1 illustrates an example of the single- and binary star regions we defined for the Pleiades cluster.

In this study, we quantify the binary fraction of systems with a mass ratio $q > q_0 = 0.4$. This is achieved by computing the ratio between the total number of binary systems and the overall number of stars within the selected regions:

$$f_{\rm bin}^{q>0.4} = \frac{N_{\rm bin}}{(N_{\rm sin} + N_{\rm bin})}, \tag{1}$$

where $N_{\rm bin}$ and $N_{\rm sin}$ are the number of binary systems and single stars, respectively. The fractions of binaries with $q > 0.4$, $f_{\rm bin}^{q>0.4}$, for all 85 open clusters are presented in column (5) of Table 1. In total, 1811 binary candidates are identified among the target clusters. Only two of them are crossmatched with the non-single-star catalog published by Gaia DR3 (Gaia Collaboration et al. 2022) that was determined via spectra.

The accuracy of our binary content analysis can be affected by contamination from field stars, particularly for faint stars with masses below 0.5 $M_\odot$. The global contamination rate of member stars is limited to 5% (Pang et al. 2022b), which mainly affects stars fainter than the binary selection regions. The field star contamination in the binary selection region (as shown in Figure 1) is even lower than 5%. Therefore, our binary candidates are statistically robust. The selection of binaries in the CMD is advantageous in efficiency and independent of influence by the orbital period or inclination angles of the binary systems (Milone et al. 2012). Most of our target clusters are consistent with a uniform extinction; we adopt the best-fitting extinction value from isochrone fitting in Pang et al. (2021a, 2021b, 2022b) and Li et al. (2021) for the members of each cluster.

3.2. Error Estimation

The mean photometric uncertainty of Gaia DR3 is about 1 mmag (Gaia Collaboration et al. 2022), which may result in uncertain placement of cluster members in the CMD and may lead to variations in the number of measured single or binary stars (as shown by the gray dots in Figure 1(c)). To account for this effect, we simulate the impact of observational photometric uncertainty by assigning each member a new magnitude drawn from a Gaussian distribution centered at the observed value and with a dispersion of the photometric uncertainty of the individual star. With the updated locations of each member in the CMD, we then measure the number of stars within the single and binary regions again and recalculate the binary fraction using Equation (1). This procedure is repeated 2000 times, and the average difference between the newly obtained binary fraction and the original one from Section 3.1 is considered as the associated error of the binary fraction $f_{\rm bin}^{q>0.4}$.

3.3. Completeness Correction

Our method for identifying unresolved binary candidates is subject to bias, due to the limited angular resolution of Gaia in resolving binary systems. We apply a minimum angular separation for two-parameter solutions of $0\farcs6$ (Lindegren et al. 2021) to our sample of member stars. When the separation between the two binary components is below $0\farcs6$, the system is considered to be an unresolved binary in Gaia data.

The projected separation between the two components of a binary system at a given moment in time depends on the semimajor axis, the eccentricity, the spatial orientation of the orbit, and the orbital phase. For an ensemble of randomly oriented binary systems with identical semimajor axis a and eccentricity e, the average projected separation is

$$\overline{\rho} = \frac{\pi}{4} a \left(1 + \frac{e^2}{2}\right), \tag{2}$$

which ranges from $\overline{\rho} \approx 0.79a$ for circular orbits to $\overline{\rho} \approx 1.18a$ for near-parabolic orbits (see Section 4.3.1 in Kouwenhoven 2006 for details). In this study, we assume that the binary separation is approximately equal to the semimajor axis of the system.

The identification of unresolved binaries through the CMD in Section 3.1 is only able to recover those systems with semimajor axes smaller than the threshold value $0\farcs6$. However, binary systems with a separation larger than the minimum value are resolved as two single stars, which are not included in our estimation. This bias is particularly pronounced in nearby clusters, since significant fractions of their binary systems are resolved. This effect is demonstrated in Figure 2(a), where the binary fraction $f_{\rm bin}^{q>0.4}$ increases with cluster distance. Consequently, the binary fractions of nearby clusters are underestimated.

To estimate the completeness fraction of our identified binary candidates, we adopt a lognormal probability density function to describe the distribution of the semimajor axis for FGK stars, taken from Raghavan et al. (2010), given that our target binary candidates are primarily FGK stars. The binary population in the Galactic field is primarily composed of binaries that originate from star clusters and stellar groups. While the filamentary young stellar groups are dispersing, their binary populations likely have a higher wide binary fraction than those of old star clusters, in which binary stars have been dynamically processed for a longer period. Therefore, the properties of the binary population in the field are the result of

Table 1
Binary Fraction of 85 Open Clusters

Cluster (1)	$M_{\rm cl}$ ($M_\odot$) (2)	Age (Myr) (3)	Dist. (pc) (4)	$f_{\rm bin}^{q>0.4}$ (%) (5)	$f_{\rm binc}^{q>0.4}$ (%) (6)	$f_{\rm k07}^{\rm tot}$ (%) (7)	$f_{\rm f05}^{\rm tot}$ (%) (8)	$f_{\rm uni}^{\rm tot}$ (%) (9)
ASCC 16	241	10	346.4	11.8 ± 1.0	17.6 ± 1.4	41.9 ± 3.3	26.3 ± 2.1	29.3 ± 2.3
ASCC 19	197	8	354.7	13.3 ± 1.2	19.0 ± 1.8	45.2 ± 4.3	28.4 ± 2.7	31.7 ± 3.0
ASCC 58	254	52	477.1	14.0 ± 1.2	19.4 ± 1.9	46.2 ± 4.5	29.0 ± 2.8	32.3 ± 3.2
ASCC 105	67	73	557.8	10.0 ± 1.9	13.5 ± 2.9	32.1 ± 6.9	20.1 ± 4.3	22.5 ± 4.8
ASCC 127	182	14	374.4	14.5 ± 1.6	20.8 ± 2.1	49.5 ± 5.0	31.0 ± 3.1	34.7 ± 3.5
Alessi 3	123	631	277.3	20.6 ± 0.6	30.8 ± 0.8	73.3 ± 1.9	46.0 ± 1.2	51.3 ± 1.3
Alessi 5	242	52	397.7	11.7 ± 0.8	16.7 ± 1.1	39.8 ± 2.6	24.9 ± 1.6	27.8 ± 1.8
Alessi 9	61	265	207.6	23.8 ± 0.6	38.1 ± 0.8	90.7 ± 1.9	56.9 ± 1.2	63.5 ± 1.3
Alessi 20	241	8	423.4	20.4 ± 2.1	29.2 ± 3.0	69.5 ± 7.1	43.6 ± 4.5	48.7 ± 5.0
Alessi 20 gp1	172	11	411.9	21.9 ± 1.7	31.4 ± 2.4	74.8 ± 5.7	46.9 ± 3.6	52.3 ± 4.0
Alessi 20 isl1	97	100	458.9	10.9 ± 1.4	15.1 ± 2.0	36.0 ± 4.8	22.5 ± 3.0	25.2 ± 3.3
Alessi 24	119	87	484.4	14.5 ± 6.2	20.1 ± 8.3	47.9 ± 19.8	30.0 ± 12.4	33.5 ± 13.8
Alessi 62	143	692	618.9	21.3 ± 3.7	28.9 ± 4.8	68.8 ± 11.4	43.1 ± 7.2	48.2 ± 8.0
BH 99	565	81	446.9	11.8 ± 1.9	16.9 ± 2.7	40.2 ± 6.4	25.2 ± 4.0	28.2 ± 4.5
BH 164	196	64	420.2	12.9 ± 4.1	18.5 ± 5.6	44.0 ± 13.3	27.6 ± 8.4	30.8 ± 9.3
Blanco 1	338	100	236.8	11.0 ± 0.6	17.6 ± 0.9	41.9 ± 2.1	26.3 ± 1.3	29.3± 1.5
Collinder 69	401	13	398.9	33.9 ± 1.4	48.5 ± 2.1	115.5 ± 5.0	72.4 ± 3.1	80.8 ± 3.5
Collinder 135	251	40	303.2	18.3 ± 1.0	27.4 ± 1.5	65.2 ± 3.6	40.9 ± 2.2	45.7 ± 2.5
Collinder 140	179	49	384.5	13.2 ± 1.3	18.9 ± 1.8	45.0 ± 4.3	28.2 ± 2.7	31.5 ± 3.0
Collinder 350	149	589	367.9	28.0 ± 2.1	40.1 ± 2.8	95.5 ± 6.7	59.9 ± 4.2	66.8 ± 4.7
Coma Berenices	100	700	86.0	4.2 ± 0.2	7.7 ± 0.5	18.3 ± 1.2	11.5 ± 0.7	12.8 ± 0.8
Group X	98	400	99.6	8.9 ± 0.4	16.3 ± 0.8	38.8 ± 1.9	24.3 ± 1.2	27.2 ± 1.3
Gulliver 6	169	7	413.3	16.9 ± 1.5	24.2 ± 2.2	57.6 ± 5.2	36.1 ± 3.3	40.3 ± 3.7
Gulliver 21	83	274	652.5	15.7 ± 2.6	21.3 ± 3.7	50.7 ± 8.8	31.8 ± 5.5	35.5 ± 6.2
Huluwa 1	724	12	355.1	16.3 ± 0.5	23.3 ± 0.8	55.5 ± 1.9	34.8 ± 1.2	38.8 ± 1.3
Huluwa 2	469	11	399.0	17.3 ± 0.9	24.8 ± 1.2	59.0 ± 2.9	37.0 ± 1.8	41.3 ± 2.0
Huluwa 3	371	10	394.6	15.4 ± 0.9	22.0 ± 1.2	52.4 ± 2.9	32.8 ± 1.8	36.7 ± 2.0
Huluwa 4	181	10	342.1	19.4 ± 0.8	29.0 ± 1.2	69.0 ± 2.9	43.3 ± 1.8	48.3 ± 2.0
Huluwa 5	60	7	354.6	4.0 ± 1.8	5.7 ± 2.4	13.6 ± 5.7	8.5 ± 3.6	9.5 ± 4.0
IC 348	142	4	316.5	30.3 ± 1.9	45.3 ± 2.8	107.9 ± 6.7	67.6 ± 4.2	75.5 ± 4.7
IC 2391	138	49	151.3	9.7 ± 0.7	15.5 ± 1.0	36.9 ± 2.4	23.1 ± 1.5	25.8 ± 1.7
IC 2602	187	44	151.4	8.5 ± 0.6	13.6 ± 1.0	32.4 ± 2.4	20.3 ± 1.5	22.7 ± 1.7
IC 4665	159	35	347.2	13.0 ± 1.2	19.4 ± 1.9	46.2 ± 4.5	29.0 ± 2.8	32.3 ± 3.2
IC 4756	509	954	473.7	16.6 ± 1.0	23.0 ± 1.3	54.8 ± 3.1	34.3 ± 1.9	38.3 ± 2.2
LP 2371	81	19	366.9	12.5 ± 2.3	17.9 ± 3.7	42.6 ± 8.8	26.7 ± 5.5	29.8 ± 6.2
LP 2373	98	4	386.9	26.3 ± 3.2	37.7 ± 4.3	89.8 ± 10.2	56.3 ± 6.4	62.8 ± 7.2
LP 2373 gp1	186	10	335.6	18.2 ± 1.2	27.2 ± 1.8	64.8 ± 4.3	40.6 ± 2.7	45.3 ± 3.0
LP 2373 gp2	544	8	349.3	15.4 ± 0.9	23.0 ± 1.4	54.8 ± 3.3	34.3 ± 2.1	38.3 ± 2.3
LP 2373 gp3	111	6	349.0	11.9 ± 2.5	17.8 ± 3.9	42.4 ± 9.3	26.6 ± 5.8	29.7 ± 6.5
LP 2373 gp4	295	6	363.0	17.6 ± 0.9	25.2 ± 1.4	60.0 ± 3.3	37.6 ± 2.1	42.0 ± 2.3
LP 2383	277	49	363.5	12.1 ± 1.1	17.3 ± 1.6	41.2 ± 3.8	25.8 ± 2.4	28.8 ± 2.7
LP 2388	149	21	497.3	34.5 ± 2.6	47.9 ± 3.6	114.0 ± 8.6	71.5 ± 5.4	79.8 ± 6.0
LP 2428	112	200	436.0	37.4 ± 1.8	53.5 ± 2.6	127.4 ± 6.2	79.9 ± 3.9	89.2 ± 4.3
LP 2429	148	1150	479.9	18.5 ± 1.0	25.7 ± 1.3	61.2 ± 3.1	38.4 ± 1.9	42.8 ± 2.2
LP 2439	141	24	283.7	11.4 ± 0.8	17.0 ± 1.3	40.5 ± 3.1	25.4 ± 1.9	28.3 ± 2.2
LP 2441	187	74	280.6	18.5 ± 1.0	27.7 ± 1.6	66.0 ± 3.8	41.3 ± 2.4	46.2 ± 2.7
LP 2442	318	14	176.2	10.4 ± 0.5	16.6 ± 1.0	39.5 ± 2.4	24.8 ± 1.5	27.7 ± 1.7
LP 2442 gp1	111	8	139.2	14.8 ± 1.9	27.0 ± 3.6	64.3 ± 8.6	40.3 ± 5.4	45.0 ± 6.0
LP 2442 gp2	151	8	140.5	24.1 ± 2.0	44.0 ± 4.0	104.8 ± 9.5	65.7 ± 6.0	73.3 ± 6.7
LP 2442 gp3	64	8	142.4	13.8 ± 2.4	25.2 ± 4.5	60.0 ± 10.7	37.6 ± 6.7	42.0 ± 7.5
LP 2442 gp4	113	8	153.7	22.2 ± 1.8	35.5 ± 2.9	84.5 ± 6.9	53.0 ± 4.3	59.2 ± 4.8
LP 2442 gp5	76	8	154.1	12.5 ± 0.1	20.0 ± 0.2	47.6 ± 0.5	29.9 ± 0.3	33.3 ± 0.3
Mamajek 4	282	371	449.9	9.9 ± 1.6	14.2 ± 2.3	33.8 ± 5.5	21.2 ± 3.4	23.7 ± 3.8
NGC 1901	124	850	418.3	32.9 ± 1.4	47.1 ± 2.0	112.1 ± 4.8	70.3 ± 3.0	78.5 ± 3.3
NGC 1977	108	3	392.3	16.1 ± 1.7	23.0 ± 2.5	54.8 ± 6.0	34.3 ± 3.7	38.3 ± 4.2
NGC 1980	757	5	383.6	22.0 ± 0.8	31.5 ± 1.2	75.0 ± 2.9	47.0 ± 1.8	52.5 ± 2.0
NGC 2232	205	24	319.6	13.1 ± 1.0	19.6 ± 1.5	46.7 ± 3.6	29.3 ± 2.2	32.7 ± 2.5
NGC 2422	477	72	476.4	4.2 ± 0.5	5.8 ± 0.7	13.8 ± 1.7	8.7 ± 1.0	9.7 ± 1.2
NGC 2451A	178	57	192.5	16.2 ± 0.9	25.9 ± 1.5	61.7 ± 3.6	38.7 ± 2.2	43.2 ± 2.5
NGC 2451B	276	49	363.3	15.9 ± 1.1	22.8 ± 1.6	54.3 ± 3.8	34.0 ± 2.4	38.0 ± 2.7
NGC 2516	1984	123	410.6	12.4 ± 0.3	17.8 ± 0.5	42.4 ± 1.2	26.6 ± 0.7	29.7 ± 0.8
NGC 2547	302	39	387.1	14.0 ± 1.3	20.0 ± 1.7	47.6 ± 4.0	29.9 ± 2.5	33.3 ± 2.8

Table 1
(Continued)

Cluster (1)	$M_{\rm cl}$ ($M_\odot$) (2)	Age (Myr) (3)	Dist. (pc) (4)	$f_{\rm bin}^{q>0.4}$ (%) (5)	$f_{\rm binc}^{q>0.4}$ (%) (6)	$f_{\rm k07}^{\rm tot}$ (%) (7)	$f_{\rm f05}^{\rm tot}$ (%) (8)	$f_{\rm uni}^{\rm tot}$ (%) (9)
NGC 3228	84	62	482.2	34.1 ± 4.2	47.3 ± 6.2	112.6 ± 14.8	70.6 ± 9.3	78.8 ± 10.3
NGC 3532	2228	397	478.3	11.4 ± 1.2	15.8 ± 1.8	37.6 ± 4.3	23.6 ± 2.7	26.3 ± 3.0
NGC 6405	598	79	457.6	15.8 ± 1.8	21.9 ± 2.6	52.1 ± 6.2	32.7 ± 3.9	36.5 ± 4.3
NGC 6475	1023	185	279.5	9.3 ± 0.4	13.9 ± 0.5	33.1 ±1.2	20.7 ± 0.7	23.2 ± 0.8
NGC 6633	338	426	393.8	12.6 ± 1.0	18.0 ± 1.3	42.9 ± 3.1	26.9 ± 1.9	30.0 ± 2.2
NGC 6774	152	2650	306.1	15.9 ± 1.3	23.8 ± 1.8	56.7 ± 4.3	35.5 ± 2.7	39.7 ± 3.0
NGC 7058	126	80	365.2	10.4 ± 1.5	14.9 ± 2.1	35.5 ± 5.0	22.2 ± 3.1	24.8 ± 3.5
NGC 7092	191	350	297.1	8.5 ± 1.0	12.7 ± 1.4	30.2 ± 3.3	19.0 ± 2.1	21.2 ± 2.3
Pleiades	740	124	135.9	10.3 ± 0.3	18.8 ± 0.5	44.8 ± 1.2	28.1 ± 0.7	31.3 ± 0.8
Praesepe	601	700	185.0	9.2 ± 0.4	14.7 ± 0.6	35.0 ± 1.4	21.9 ± 0.9	24.5 ± 1.0
RSG 7	67	70	419.3	10.5 ± 0.1	15.0 ± 0.1	35.7 ± 0.2	22.4 ± 0.1	25.0 ± 0.2
RSG 8	341	17	474.6	17.1 ± 1.0	23.7 ± 1.5	56.4 ± 3.6	35.4 ± 2.2	39.5 ± 2.5
Roslund 5	191	97	540.5	12.5 ± 1.5	17.3 ± 2.4	41.2 ± 5.7	25.8 ± 3.6	28.8 ± 4.0
Stephenson 1	262	46	358.6	10.3 ± 0.9	14.7 ± 1.2	35.0 ± 2.9	21.9 ± 1.8	24.5 ± 2.0
Stock 1	137	470	405.6	10.4 ± 0.6	14.9 ± 0.7	35.5 ± 1.7	22.2 ± 1.0	24.8 ± 1.2
Stock 12	121	112	437.8	9.7 ± 0.5	13.9 ± 0.8	33.1 ± 1.9	20.7 ± 1.2	23.2 ± 1.3
Stock 23	105	94	606.9	20.8 ± 4.3	28.2 ± 5.5	67.1 ± 13.1	42.1 ± 8.2	47.0 ± 9.2
UBC 19	42	7	399.7	26.3 ± 4.4	37.7 ± 6.8	89.8 ± 16.2	56.3 ± 10.1	62.8 ± 11.3
UBC 31	260	11	365.0	14.0 ± 1.7	20.0 ± 2.7	47.6 ± 6.4	29.9 ± 4.0	33.3 ± 4.5
UBC 31 gp1	58	11	339.1	12.0 ± 2.3	17.9 ± 3.0	42.6 ± 7.1	26.7 ± 4.5	29.8 ± 5.0
UBC 31 gp2	185	10	381.4	17.1 ± 2.4	24.5 ± 3.6	58.3 ± 8.6	36.6 ± 5.4	40.8 ± 6.0
UBC 7	191	40	278.1	10.3 ± 1.3	15.4 ± 2.0	36.7 ± 4.8	23.0 ± 3.0	25.7 ± 3.3
UPK 82	57	81	542.2	6.8 ± 2.2	9.4 ± 3.0	22.4 ± 7.1	14.0 ± 4.5	15.7 ± 5.0

Note. $M_{\rm cl}$ is the total mass of each star cluster. The age of the cluster is obtained from Pang et al. (2022b) and was derived from PARSEC isochrone fitting. Dist. is the distance after the distance correction from Pang et al. (2022b), via the Bayesian method. Columns (5) to (6) present the binary fractions of each cluster. $f_{\rm bin}^{q>0.4}$ is the binary fraction computed using Equation (1). $f_{\rm binc}^{q>0.4}$ is the binary fraction after completeness correction, as described in Section 3.3. $f_{\rm k07}^{\rm tot}$, $f_{\rm f05}^{\rm tot}$, and $f_{\rm uni}^{\rm tot}$ are the total binary fractions, assuming mass ratio distributions from Kouwenhoven et al. (2007), Fisher et al. (2005), as well as a uniform mass ratio distribution (Section 3.4).

dynamical evolution in different environments: a combination of binaries originating from old disrupting clusters and young dispersing stellar groups. Both cluster types are well represented in our sample. We therefore adopt the distributions of Raghavan et al. (2010) as an approximation for the binary stars in our sample. Note that using the distribution of Raghavan et al. (2010) overestimates the wide binary population for dense clusters. Therefore, the corresponding completeness-corrected values will be treated as upper limits for the denser clusters in our sample. The lognormal distribution of semimajor axis a has a mean value of 40 astronomical units (au) and a dispersion of $\log(a/\mathrm{au}) = 1.5$. The corresponding completeness fraction $f_{\rm comp}$ for the binary systems of each respective cluster is obtained by integrating the distribution of a up to the $0\farcs6$ separation limit from Gaia, whose physical value (in au) varies depending on the distance of the clusters (as outlined in column (3) of Table 2). As the cluster distance increases, the completeness fraction $f_{\rm comp}$ generally increases as well (as illustrated in Figure 2(b)), ranging from 0.55 to 0.75. In the nearest 100 pc neighboring region, the CMD identification method fails to detect approximately 45% of the binary population in the star cluster. The binary fraction $f_{\rm bin}^{q>0.4}$ for each cluster is adjusted by dividing the value $f_{\rm bin}^{q>0.4}$ by the corresponding completeness fraction $f_{\rm comp}$ at that distance (column (4) in Table 2). We group the target clusters into distance bins with a step size of 100 pc. Clusters in the same bin are assigned the same value of $f_{\rm comp}$. The resulting corrected binary fraction $f_{\rm binc}^{q>0.4}$ is presented in column (6) of Table 1. As shown in Figure 2(c), the dependence of binary fraction on distance is reduced after the correction, indicated by the Spearman's rank correlation coefficient, which changes from $s = 0.2$ (a) to $s = 0.05$ (c).

3.4. Total Binary Fraction

To estimate the total binary fraction, we apply an extrapolation method that involves using the binary fraction $f_{\rm bin}^{q>0.4}$ for systems with mass ratios $q > 0.4$ and applying it to binary systems with $q < 0.4$. This is achieved through the use of a given mass ratio distribution function $f(q)$. For extremely low-mass-ratio systems, the companion may be a brown dwarf or planet, instead of a star; such systems are normally not considered as stellar binary systems. Therefore, the total binary fraction obtained in this manner is considered as an upper limit. Kouwenhoven et al. (2009), however, have shown that for the spectral types considered in our sample (FGK stars), the overestimation is small for the mass ratio distributions described below. Our approach is as follows.

(1) First, we make an assumption regarding the mass ratio distribution function $f(q)$, based on the work by Kouwenhoven et al. (2007), which takes the form of

$$f(q) \propto q^{-0.4\pm0.1}. \tag{3}$$

This particular distribution is dominated by low-mass-ratio binary systems. The total binary fraction of the cluster is then estimated by multiplying the previously calculated completed binary fraction $f_{\rm binc}^{q>0.4}$ (column (6) in Table 1) with a factor 2.38 ± 0.31, which depends on this assumed $f(q)$ distribution:

$$f_{\rm k07}^{\rm tot} = (2.38 \pm 0.31) f_{\rm binc}^{q>0.4}. \tag{4}$$

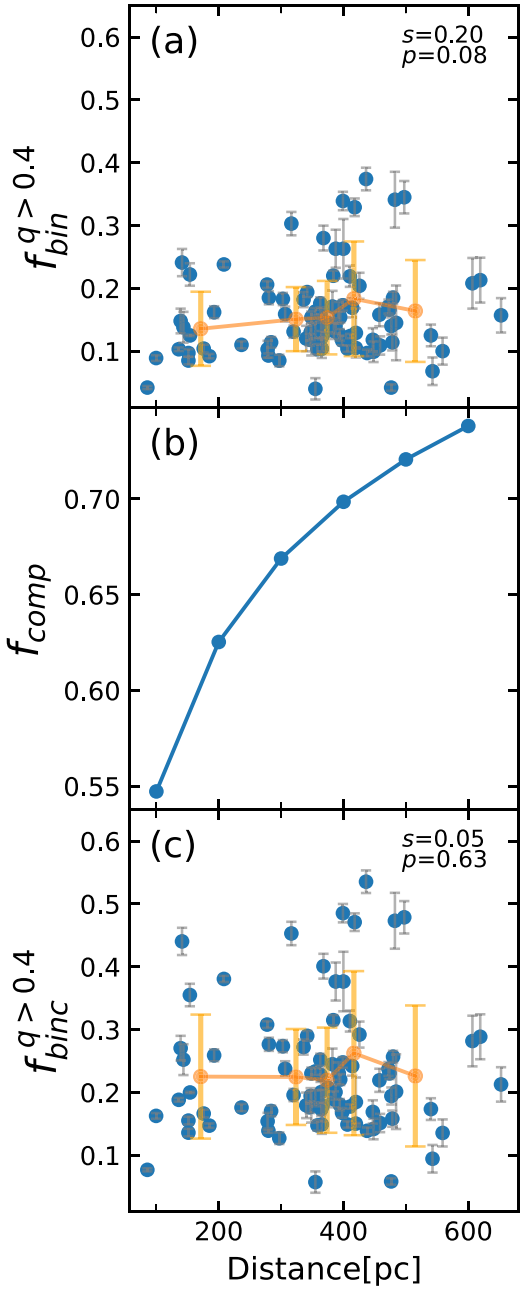

Figure 2. (a) The relation between the binary fraction for $q > 0.4$ identified in Section 3.1 (blue dots) and the distances of the clusters. The error bar of $f_{\rm bin}^{q>0.4}$ is estimated in Section 3.2. The orange dots are average values of cluster distance and $f_{\rm bin}^{q>0.4}$ for all 17 clusters in each bin, with the standard deviation indicated by the error bar. (b) Dependence of the completeness fraction on distance. $f_{\rm comp}$ is estimated from Gaia's angular resolution limit at a given distance taken from Table 2. (c) Binary fraction after incompleteness correction $f_{\rm binc}^{q>0.4}$ vs. cluster distance. The error bar of $f_{\rm binc}^{q>0.4}$ is propagated from the error estimated in Section 3.2. The computation scheme of the orange dots is identical to that in (a). The quantity s is the Spearman's rank correlation coefficient, and p is the probability of the null hypothesis (that no correlation exists between two variables) of the correlation test. A p value of less than 0.1 means that the null hypothesis is rejected.

The error from the factor is propagated to the binary fraction, which is the highest among the three mass ratio profiles. Considering this mass ratio is obtained for young associations, it may overestimate the general binary fraction for older clusters. Therefore, we will not use the total binary fraction for quantitative analysis. The resulting values are listed in column (7) of Table 1.

Table 2
Binary Separation Limit for Gaia Data at Different Distances

Distance (pc) (1)	θ (arcsec) (2)	a (au) (3)	$f_{\rm comp}$ (4)
100	0.6	60	0.55
200	0.6	120	0.63
300	0.6	180	0.67
400	0.6	240	0.70
500	0.6	300	0.72
600	0.6	360	0.74

Note. θ is the minimum angular separation for two-parameter solutions in Gaia data. a is the corresponding semimajor axis computed from θ for the binary system. $f_{\rm comp}$ is the completeness fraction for our identified binary candidates at different distances.

(2) In contrast to the mass ratio distribution assumed in Kouwenhoven et al. (2007), the distribution presented in Fisher et al. (2005) exhibits an increase in the frequency of high-mass-ratio binary systems, with a peak at around $q \sim 0.9$–1.0. Over 70% of binary stars have mass ratios greater than 0.4. Adopting the $f(q)$ distribution from Fisher et al. (2005), we estimate the total binary fraction to be

$$f_{\rm f05}^{\rm tot} = 1.49 f_{\rm binc}^{q>0.4}. \quad (5)$$

The values of $f_{\rm f05}^{\rm tot}$ (Fisher et al. 2005) are listed in column (8) of Table 1. The coefficient is obtained from the number count of the histogram in Fisher et al. (2005), for which no uncertainty is provided. We therefore do not compute the uncertainty for this mass ratio distribution. A similar procedure has been carried out by Milone et al. (2012).

(3) Assuming a uniform $f(q)$ for binary stars, the mass ratio remains constant across all values of q. Previous studies have shown that solar-type stars in the field and star cluster follow a roughly uniform distribution (Li et al. 2020; Torres et al. 2021; Offner et al. 2022). In this scenario, the total binary fraction is given by

$$f_{\rm uni}^{\rm tot} = 1.67 f_{\rm binc}^{q>0.4}, \quad (6)$$

which value is listed in the last column of Table 1. The coefficient for the uniform distribution is exact, and no uncertainty is computed. Considering the underestimated uncertainty of the total binary fraction, we do not use it for quantitative analysis in the remainder of this study. Elaborating upon the distribution of the mass ratio in a more comprehensive manner goes beyond the scope of the current study.

4. Global Binary Properties

According to the Gaia angular resolution limit (Section 3.3), the binary systems we have identified in this study are classified as intermediate to close binaries, with separations of $\leqslant$360 au (Offner et al. 2022). The survival of binary systems in clustered environments depends not only on their own energy, but also on the energy and frequency of encounters (Parker & Meyer 2014). Therefore, the hardness of the binary system, which is defined by the ratio between its binding energy and the kinetic energy of the system's center of mass

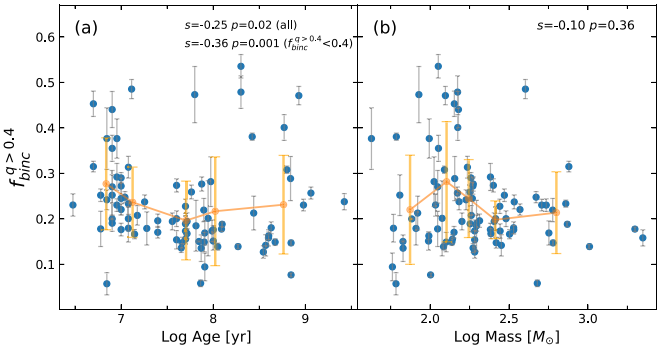

Figure 3. The relations between the completeness-corrected binary fraction for $q > 0.4$ identified in Section 3.3 and the age of the cluster (panel (a)) and the cluster total masses (panel (b)). The error bar of $f_{\rm binc}^{q>0.4}$ is propagated from the error estimated in Section 3.2. The orange dots represent the average values of the cluster distances and $f_{\rm binc}^{q>0.4}$ for all 17 clusters in each bin, with the standard deviation indicated with error bars. The Spearman's rank correlation coefficient s and the probability of the null hypothesis p are indicated in the upper right corner of each panel. The meanings of the quantities s and p are identical to those in Figure 2.

(Parker & Goodwin 2012; Reipurth et al. 2014), is of great importance. The kinetic energy of the binary system and the encounter rates, and thus the hardness, are significantly affected by the stellar density. Using the current number of members and cluster size (the half-mass radius obtained from Pang et al. 2022b), we estimate the hard–soft boundary $a_{\rm hs}$ for our cluster sample using Equation (1) as provided by Reipurth et al. (2014). The value of $a_{\rm hs}$ ranges from a few hundred au up to a few thousand au. However, due to the mass loss of the cluster and the observational incompleteness of members, this value of $a_{\rm hs}$ is an upper limit, and it was likely much smaller at the time of birth of the cluster. Therefore, the binary sample we have studied in the 85 target clusters certainly includes both soft and hard binaries.

4.1. Binary Fraction versus Age

The evolution of a cluster tends to lead to changes in the hardness of its constituent binary systems, with hard binaries becoming harder and soft binaries becoming softer (Heggie & Hut 2003). Soft binaries are likely to eventually disrupt as the cluster undergoes secular evolution, leading to a decline in the overall binary fraction as the cluster ages. Figure 3(a) depicts the relationship between the completeness-corrected binary fraction $f_{\rm binc}^{q>0.4}$ and cluster age, with a clear scatter observed across all ages. Despite the scatter among some clusters with $f_{\rm binc}^{q>0.4}$ values above 40%, the majority follow the trend of decreasing binary fraction with increasing age ($s = -0.36$). The small value of p indicates that a correlation exists between cluster age and $f_{\rm binc}^{q>0.4}$, although the Spearman's rank correlation coefficient s indicates that the degree of correlation is modest. The scatter in the binary fraction is equally large at young ages ($\leqslant$10 Myr) as it is at old ages ($\sim$1 Gyr). Young stellar groups and clusters are ideal laboratories for studying primordial binary properties. The dispersion in the binary fraction may be caused by different binary initial conditions in different clustered environments during the star formation process. As wide and soft binaries are disrupted as clusters evolve, the total number of binaries declines. At the same time, single stars also continue to escape from the cluster and consequently the total member number decreases, thus artificially pushing up the binary fraction. Therefore, the scatter of the binary fraction in old clusters provides insights into the degree of dynamical disruption of clusters.

4.2. Binary Fraction versus Cluster Mass

In the Figure 3(b), we show the dependence of the binary fraction on cluster mass. There exists an increasing trend in clusters with masses less than 200 $M_\odot$, where the binary fraction rises from 20% to 30% on average. In clusters with higher masses, the total binary fraction appears to be unaffected by the cluster mass and the scatter is also reduced. There is statistical indication of a higher binary fraction in lower-mass clusters than in higher-mass counterparts in our sample, which may be attributed to the lower stellar density in low-mass clusters. The collision rates and mean kinetic energy of colliding stars are both lower in such environments (Sollima et al. 2010). However, the Spearman's rank correlation coefficient, $s = -0.10$, suggests a weak correlation between the binary fraction and the cluster mass, similar to the results of globular clusters (Milone et al. 2012).

4.3. Binary Fraction versus Stellar Density

To explore the link between the binary fraction and stellar density in clusters, we investigate the correlation between the corrected binary fraction $f_{\rm binc}^{q>0.4}$ and the central stellar density ($r \leqslant r_{\rm h}$) in Figure 4(a). However, we do not observe an obvious dependence of binary fraction on central stellar density for any of the clusters. On the contrary, Niu et al. (2020) have found that the binary fraction increases with higher stellar density. Their 12 open clusters are all older than 100 Myr with high stellar density within $r_{\rm h}$ (ρ is in the range of 1–7 $M_\odot$ pc^{-3}). We highlight clusters older than 100 Myr in Figure 4(a) (orange dots) and conversely observe an opposite trend, that the binary fraction decreases with higher stellar density. No evident trend is observed in the clusters younger than 100 Myr (the blue dots in Figure 4(a)).

In order to study the binary fraction dependence on stellar density in the same cluster, we conduct an analysis of the radial distribution of the binary fraction in three annular regions within our sample of clusters, defined by radial distances of $r \leqslant r_{\rm h}$, $r_{\rm h} < r \leqslant 2r_{\rm h}$, and $2r_{\rm h} < r \leqslant 3r_{\rm h}$. To ensure statistically reliable outcomes, we restrict our examination to annuli comprising at least five binary candidates. We plot the mean value of the binary fraction in each density bin (with an identical number of clusters) with the dark gray dots in Figure 4(b). The vertical error bar is the standard deviation of the binary fraction in each density bin. From the outskirts to the central core region, the mean binary fraction of each bin (the dark gray dots) decreases from 25% to 15%. This reveals a noticeable decline in the binary fraction with increasing density in the same clustered environment, considering the relatively strong correlation indicated by the Spearman's rank correlation coefficient, with a value of $s = -0.78$. Among the clusters and groups in our sample, 70% are younger than 100 Myr. The decline of the binary fraction toward high-density regions is evidence of early binary disruption in young stellar systems. This is the most robust relation compared to binary fraction with age or cluster mass, indicating that stellar density is probably a fundamental parameter in determining binary evolution.

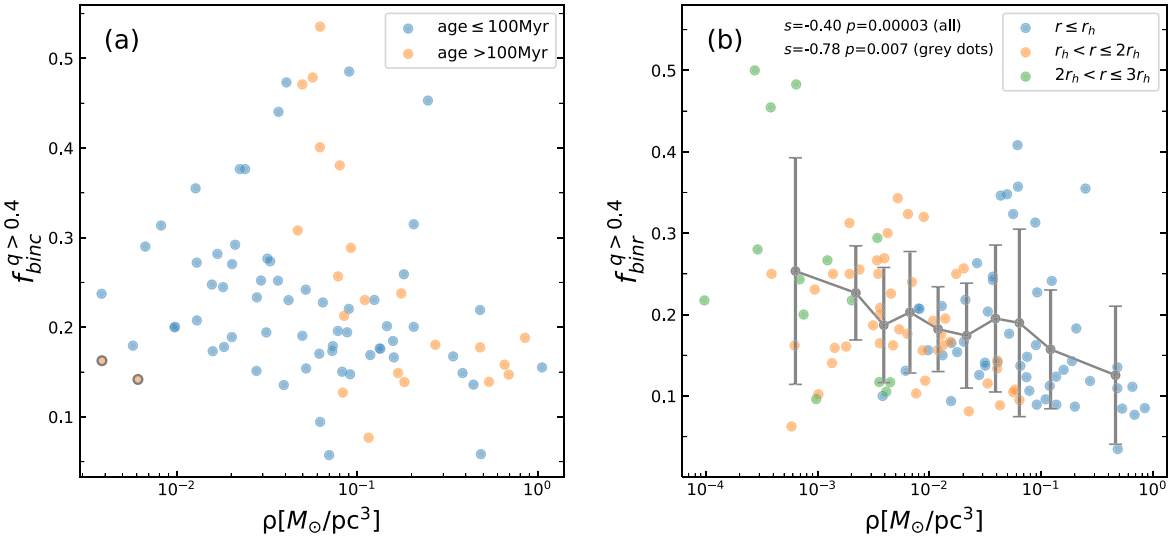

Figure 4. The correlation between the completeness-corrected binary fraction for $q > 0.4$ computed in Section 3.3 and the stellar density within the half-mass radius (a). The blue dots are clusters with ages less than 100 Myr, while the orange dots are older than 100 Myr. Two orange dots with black circles are outliers: the disrupted cluster Group X, which fragments into two overdensities, and the tidal tail cluster Mamajek 4, with very low central density. In panel (b), we display the radial binary fraction vs. the radial stellar density in each cluster, for regions with a binary number of more than five. The blue dots refer to the binary fraction and stellar density for stars within the half-mass radius r_h; the orange dots to stars between r_h and $2r_h$; and the green dots to stars between $2r_h$ and $3r_h$. The gray dots show the mean values of each bin with the same number of clusters. The vertical error bar is the standard deviation of the binary fraction in each bin. The meanings of the quantities s and p are identical to those in Figure 2.

5. Binary Fractions in Different Environments

5.1. Mean Radial Profile of Binaries

The 85 open clusters examined in this study have been classified by Pang et al. (2022b) into four distinct types, based on their morphology: filamentary, fractal, halo, and tidal tail. These four types correspond to different clustered environments. The filamentary and fractal types are both less than 100 Myr and exhibit elongated filament shapes or fractal structures, respectively. They are formed along the filaments of molecular clouds with relatively low star formation efficiency (Kruijssen 2012). The density of these clusters or groups, as seen in Figures 7 and 8 of Pang et al. (2022b), has the lowest density among the four types, making them more favorable to binary survival (Portegies Zwart et al. 2004; Parker et al. 2011). Due to their youth and low-density environments, the binary properties of the young filamentary and fractal groups are most similar to those of primordial binaries.

On the contrary, halo-type clusters are characterized by a high-density core and are the most massive and dense clusters in our sample. The high interaction rate within this dense environment disrupts binary evolution. At the same time, violent stellar encounters in the dense environment can foster the tidal capture of companions and the formation of close binaries. This mechanism is more likely to occur for massive stars (Torniamenti et al. 2022).

Finally, the tidal tail clusters represent dynamically evolved clustered environments, where the binary stars that have survived the cluster's evolution have already undergone a few or dozen relaxation times. The current stellar density within tidal tail clusters ranges from intermediate to low density. The binary members in these clusters are likely on their way to leaving the cluster, and we expect that the observed binary properties of this type of cluster should be somewhat similar to those of field binaries.

The results of our analysis reveal that filamentary and fractal types have the highest global binary fraction, with averages of $23.6\% \pm 9.2\%$ and $23.2\% \pm 7.2\%$, respectively. Tidal tail clusters or groups have a slightly lower average binary fraction of $20.8\% \pm 9.5\%$, ranking second in terms of the completeness-corrected binary fraction $f_{\rm binc}^{q>0.4}$. On the other hand, the halo-type clusters in our study exhibit the lowest binary fraction among the four types, with a mean of $14.8\% \pm 9.5\%$. These findings are consistent with theoretical predictions that low-density clustered environments are more favorable for binary survival and therefore have a higher binary fraction (Portegies Zwart et al. 2001; Parker & Meyer 2014).

In order to investigate the influence of the local stellar density on the binary fraction within each cluster or group, we conduct an analysis of the radial distribution of binary stars in different clustered environments, as shown in Figure 5. We define the regions in each cluster or group based on the dynamical scale, specifically the half-mass radius r_h, with three annuli considered: $r \leqslant r_h$, $r_h < r \leqslant 2r_h$, and $2r_h < r \leqslant 3r_h$. Our results indicate that the radial binary fraction for each of the four morphological types agrees with the global mean value, and that all types exhibit a decline in binary fraction toward the center of the cluster or group, where the density is highest. These findings are consistent with those presented in Figure 4 and suggest that local stellar density plays a critical role in shaping the binary evolution in different clustered environments.

As pointed out by Parker et al. (2011), binary systems in subvirial and substructured star clusters will experience a fast rate of dynamical processing in local dense regions, which are formed during the phase of cool collapse. The highly energetic dynamical interactions that occur in dense regions can efficiently disrupt soft binaries. Moreover, even in the expanding stellar groups, i.e., the filamentary and fractal-type clusters, local overdensity regions might dynamically process primordial binaries. Consequently, the binary populations in these clusters may have processed, and their properties may thus be different from those at birth. As our current data do not allow us to quantify the dynamical history of the targeted stellar

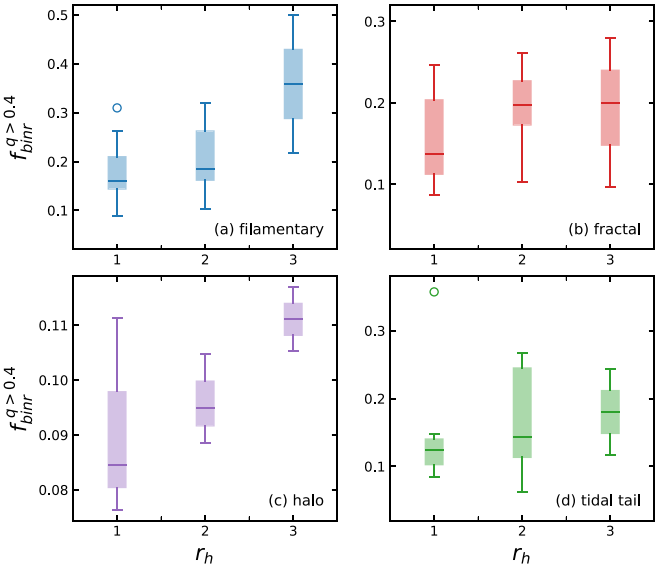

Figure 5. The dependence of the radial binary fraction on clustercentric distance in the unit of half-mass radius r_h in four types of clusters: filamentary (a), fractal (b), halo (c), and tidal tail (d). The three colored rectangles for each type indicate the values for stars within r_h, between r_h and $2r_h$, and between $2r_h$ and $3r_h$. The colored rectangles indicate the inner quartile range (IQR, 75th percentile minus 25th percentile). The median value is indicated with a horizontal line. The upper and lower whiskers of each colored rectangle mark the maximum and minimum values within 1.5 IQR. Clusters outside 1.5 IQR (whiskers) are outliers indicated as open circles: Collinder 69 (blue circle) and Collinder 350 (green circle).

groups/clusters, we cannot draw conclusive remarks on this issue.

5.2. Binary Radial Profile for Individual Clusters

For demonstration purposes, we select clusters from each morphological type that contain more than 28 binary candidates (total members >56) and plot their radial binary profiles in Figure 6. The width of the annulus is the half-mass radius r_h. As expected from the global relation shown in Figure 5 for all morphological types, the radial binary fraction is lowest inside the half-mass radius and gradually increases toward the outer part of the cluster. This is a result of the disruptive effects of dynamical evolution, which causes a significant fraction of soft binaries to be destroyed in the cluster center due to encounters. We witness early binary disruption in open clusters.

A similar trend is observed in the star cluster NGC 1818, in which the binary fraction declines toward the core (de Grijs et al. 2013; Li et al. 2013; Geller et al. 2015). For a cluster born with soft or wide binaries, the early evolution of the binary population is dominated by disruption, which decreases the overall binary frequency and establishes a decreasing trend in binary fraction toward the cluster core within approximately a crossing time. The simulations of Geller et al. (2013) have shown that a binary fraction evolves over time from one that decreases toward the core to a bimodal distribution, then eventually to a distribution that increases only toward the core, which is observed in dynamically old star clusters (Milone et al. 2012; Geller et al. 2015). This evolution process occurs over the two-body relaxation timescale. Two of the clusters in our sample (LP 2429 and NGC 6774) are older than 1 Gyr and already unbound, disrupted, and forming tidal tails. Both singles and binaries are leaving the system. Their radial profiles of binaries follow the general trend we find in Figure 6. We do not find evidence of a peak of binary fraction in the cores of these two old clusters. Due to the persistent tidal field on the Galaxy, open clusters typically become unbound and dissolve within 100–200 Myr (Dinnbier & Kroupa 2020). Binaries often escape the cluster before they reach the center. Therefore, a bound system is the precondition for maintaining binary stars and nurturing central binary evolution.

5.3. Mass Segregation in Different Environments

As clusters evolve, they experience two-body relaxation, leading to mass segregation, which is more significant in dynamically evolved systems. Since binaries are typically more massive than single stars, they tend to sink to the cluster center faster, due to the inverse proportionality between the segregation timescale and stellar mass (Pang et al. 2013). The higher-mass binaries undergo dynamical friction and mass segregation processes at a faster rate than the low-mass binaries and, therefore, although all binaries are subject to dynamical disruption early on, the higher-mass binaries begin increasing their core binary frequency more quickly (Geller et al. 2015).

We study the mass segregation of four types of clusters or groups by calculating the average stellar mass in different annuli with a size of half-mass radius r_h, as shown in Figure 7. We detect no mass segregation in the filamentary and fractal types. Interestingly, these types of young stellar groups seem to exhibit reverse segregation, where higher-mass stars are located farther away from the center. However, due to their irregular and extended morphology, the median position of the members might not accurately represent the group center. On the other hand, the most significant mass segregation is observed in the halo cluster NGC 6475, while a less pronounced but still observable amount of mass segregation is found in the halo cluster Praesepe and the tidal tail clusters IC 4756 and Pleiades, which is consistent with findings from previous studies of the same clusters (Lodieu et al. 2019; Röser & Schilbach 2019; Ye et al. 2021).

Since the filamentary and fractal stellar groups and the tidal tail clusters are extended in space, the approach of using spherical annuli may not be suitable to quantify the spatial mass distribution. In Pang et al. (2021a, 2022b), the 3D morphology of open clusters is quantified by a fitted ellipsoid. The direction of the semimajor axis d_a is considered as the elongated direction of the star cluster. Because the stellar distances from inverting the parallax generate an apparent stretching along the line of sight, the 3D X, Y, Z coordinates of each star from Pang et al. (2022b) were corrected. Pang et al. (2020, 2021a, 2022b) mitigated this problem via a Bayesian approach developed by Carrera et al. (2019), which adopted two priors: a normal distribution for the individual distances to the cluster stars and an exponentially decreasing profile for the distances to the field stars (Bailer-Jones 2015). The error for the corrected distance ranges from 0.3 to 6 pc, depending on the orientation of the primordial shape of the cluster relative to the line of sight (the primordial shape of the cluster may be spherical or elongated along the line of sight; Pang et al. 2021a).

We convert the 3D position of each star from Galactic coordinates into the Cartesian coordinates of d_a (the semimajor axis of the best-fitted ellipsoid), d_b (the semimediate axis of the best-fitted ellipsoid), and d_c (the semiminor axis of the best-fitted ellipsoid), with the origin of the coordinates located at the cluster center (the median position of all members). In Figure 8, we show the stellar mass function of three regions along the direction of the semimajor axis (d_a): the inner region with $|d_a|$

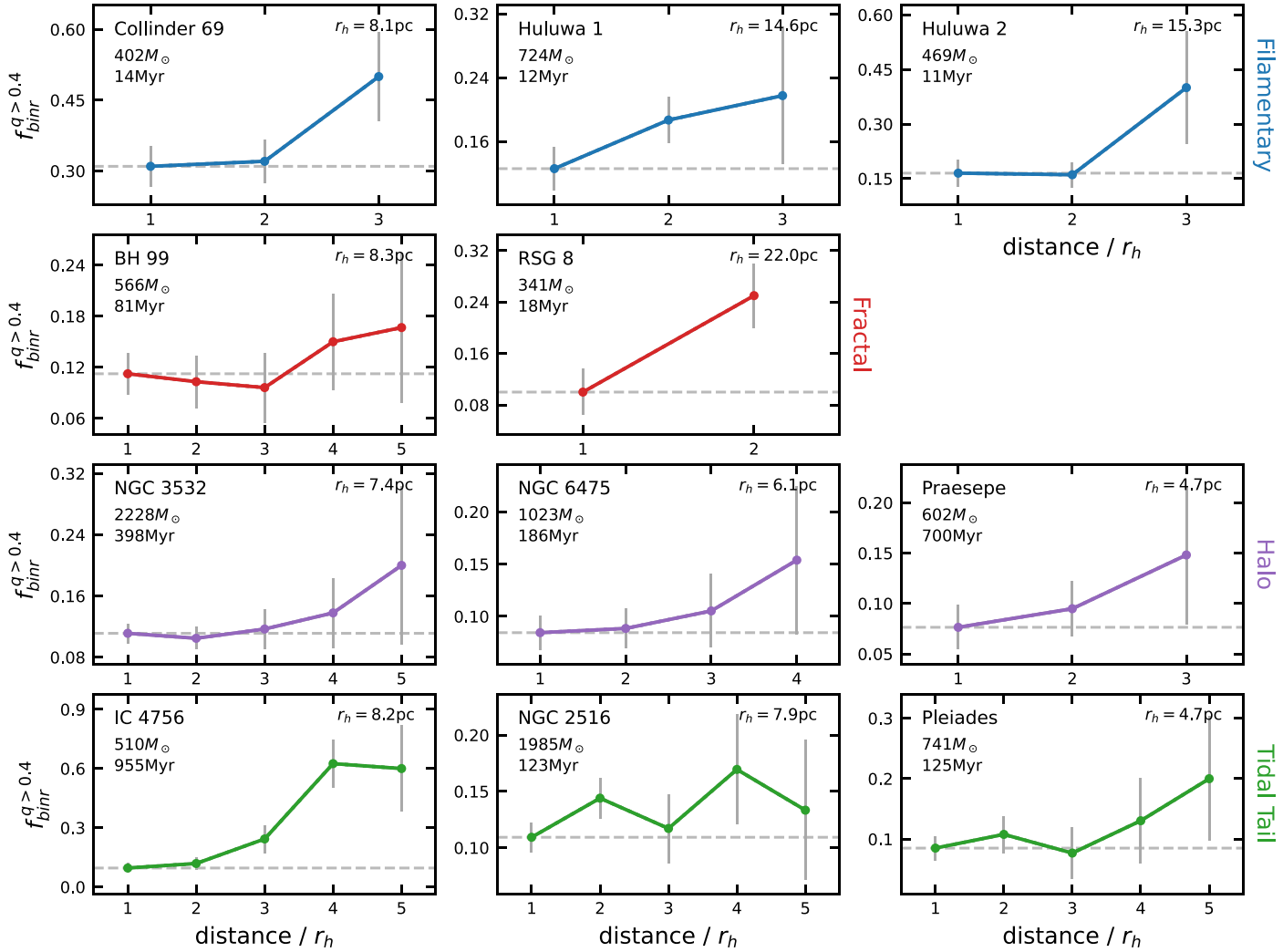

Figure 6. The radial dependence of the binary fraction on the clustercentric distance for the representative clusters of each of the four morphological types. These clusters are selected based on the number of both binary and single stars being greater than 28. The clustercentric distance is in the unit of half-mass radius $r_{\rm h}$. The types of clusters are marked with different colors. The horizontal dashed line indicates the value of $f_{\rm binr}^{q>0.4}$ for the first bin (within $r_{\rm h}$). The gray bars indicate the errors of the binary fraction of each annulus, which is the standard deviation of the sampling distribution of the binary fraction. The color coding is identical to that in Figure 5.

less than a few parsecs, and two regions on the left side (negative d_a values) and right side (positive d_a values) of the inner region. The size of each region is selected in order to ensure that the numbers of stars in each region are similar, so that they are equally statistically significant. We find hints of flatter slopes of the mass function, α (indicated in the upper right corner of each panel in Figure 8), in the inner regions of the clusters BH 99, RSG 8 (fractal type), Praesepe (halo type), and NGC 2516 (tidal tail type) than in their outer regions, providing evidence for mass segregation. Considering the uncertainty of α, the observed mass segregation is not significant. However, in the filamentary clusters, no mass segregation is observed. Instead, in these clusters, some high-mass stars are located beyond the central region of the cluster, which could be considered as inverse mass segregation.

6. Velocity Dispersions

To quantitatively analyze the internal dynamical properties of our target clusters, we compute the dispersion of the proper motion (PM) of the cluster members within and outside $r_{\rm h}$, with the goal of identifying differences in the kinematic features of stars inside and outside $r_{\rm h}$. We divide the cluster members into two groups based on their location: within or beyond $r_{\rm h}$.

We utilize the Markov Chain Monte Carlo (MCMC) method to obtain the optimal values and associated uncertainties for the PM dispersions. We model the likelihood function of the PM distribution ($\mu_\alpha \cos\delta$ and μ_δ) by two Gaussian functions (Equations (1)–(3) in Pang et al. 2018): one for the cluster members and the other for the field component (which contributes only 5% to the overall distribution).

Figure 9 displays the 1D velocity dispersion for the tangential velocity along the R.A. and decl., which are converted from PM velocity dispersions based on the distance of each cluster. The open circles correspond to values obtained from stars located inside $r_{\rm h}$, while the triangles represent those outside $r_{\rm h}$. Taking into account the uncertainty, the velocity dispersions generally exhibit isotropy along the two tangential velocity components. The mean 1D dispersion for members outside $r_{\rm h}$ is approximately 0.14–0.16 km s^{-1} larger than that inside $r_{\rm h}$. As demonstrated in Figures 4–6, the binary fraction is higher outside $r_{\rm h}$, indicating that the effects of binaries on PM measurements should be considered.

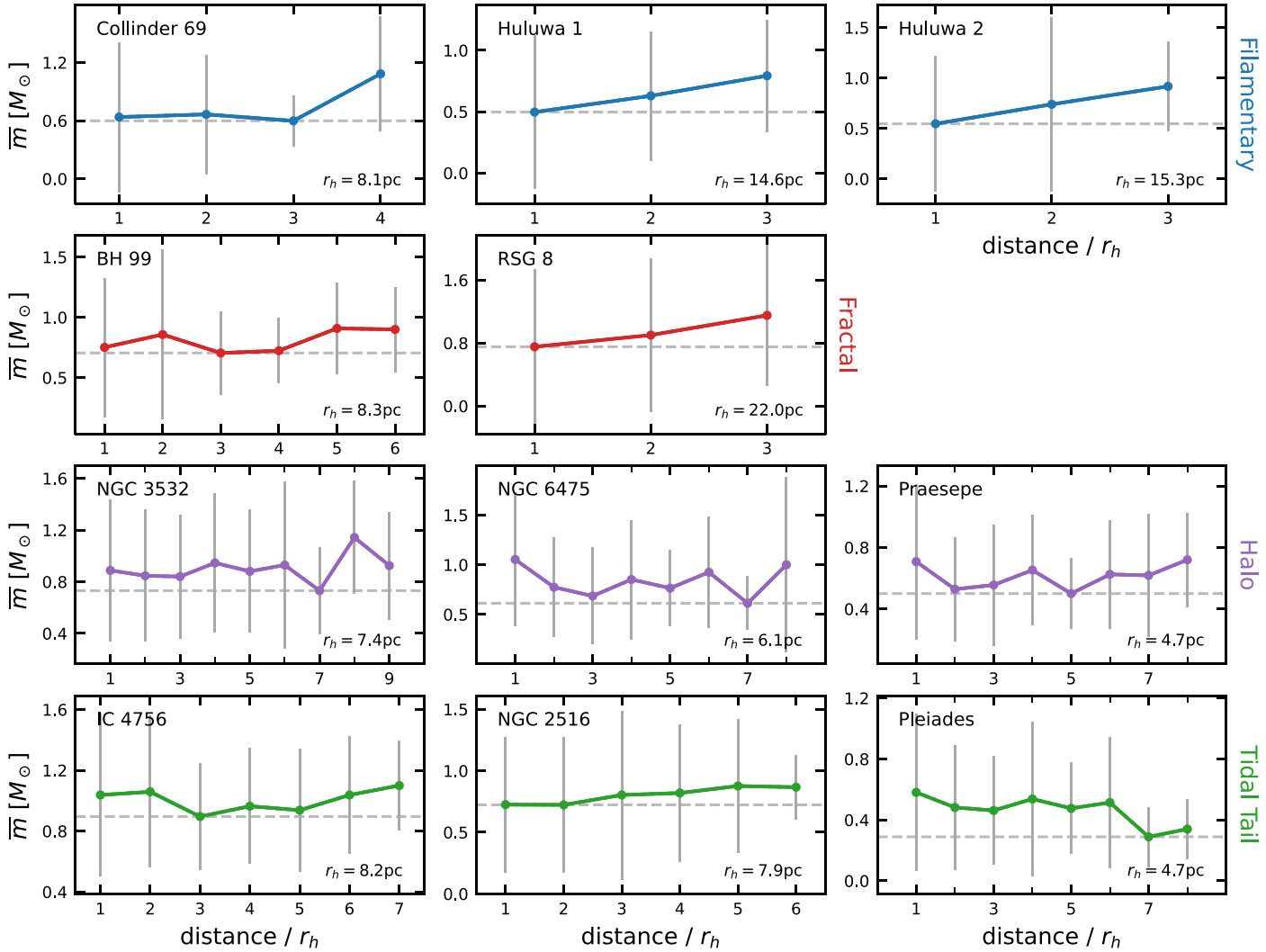

Figure 7. The dependence of the mean mass on clustercentric distance for the representative clusters of each of the four types shown in Figure 6. The size of each annulus is the half-mass radius r_h of each cluster. Each dot represents the mean mass in the annulus, and the error bar indicates the standard deviation in each bin. The horizontal dashed line indicates the smallest mean mass value among all bins. The color coding is identical to that of Figure 6.

6.1. Influence of Binaries on Velocity Dispersion

Within the typical time span of an observational campaign, a single star follows a linear and uniform trajectory in the sky. The point at which its light is concentrated, known as the photocenter, corresponds to the location of the star. In the case of an unresolved binary system, both stars orbit around their common barycenter, which does not necessarily coincide with the location of the photocenter. When the mass ratio is low, the location of the photocenter of the system is near the position of the primary star and therefore significantly deviates from the location of the barycenter. When Gaia observes the displacement of the photocenter of an unresolved binary system, it exhibits an astrometric wobble or anomaly (Wang et al. 2022), which affects the accuracy of the PM measurements and increases their uncertainty. The primary astrometric data of Gaia's current releases are obtained by treating all objects as single stars (Lindegren et al. 2021). Binary candidacy is indicated by a high renormalized unit weight error (RUWE). We compute the mean value of RUWE for binary candidates and single members in our 85 target clusters. The mean RUWE for binaries is 1.6, compared to 1.1 for singles, which tends to confirm the candidacy of the identified binaries.

We carry out a simulation to estimate the bias in the 1D tangential velocity ΔV_t along the decl. due to the deviation of the photocenter from the barycenter induced by the unresolved binary systems. The main motivation for the binary simulation is to estimate the influence of unresolved binary systems on the measurements of PM and to quantify the uncertainty in the tangential velocity dispersion measurements due to unresolved binary systems. In the case of an unresolved binary, Gaia measures the astrometry of the photocenter instead of that of the barycenter. The cluster velocity dispersion should be determined using the barycenter of the cluster. The photocentric motion will contribute a small fraction to the total velocity dispersion, and the measured velocity dispersion should thus be corrected for this effect.

In this simulation, we adopt a mass of 1 $M_\odot$ for the primary star. Given the mass ratio q, the mass of the secondary is then $qM_\odot$. Light emitted by the secondary is considered in this simulation. The position of the binary system is randomly assigned within a sphere of unit radius. We do not make any assumption about the distance to the cluster. For a binary system with a certain mass ratio and separation, we calculate the 2D projection of the nonlinear motion of the photocenter on

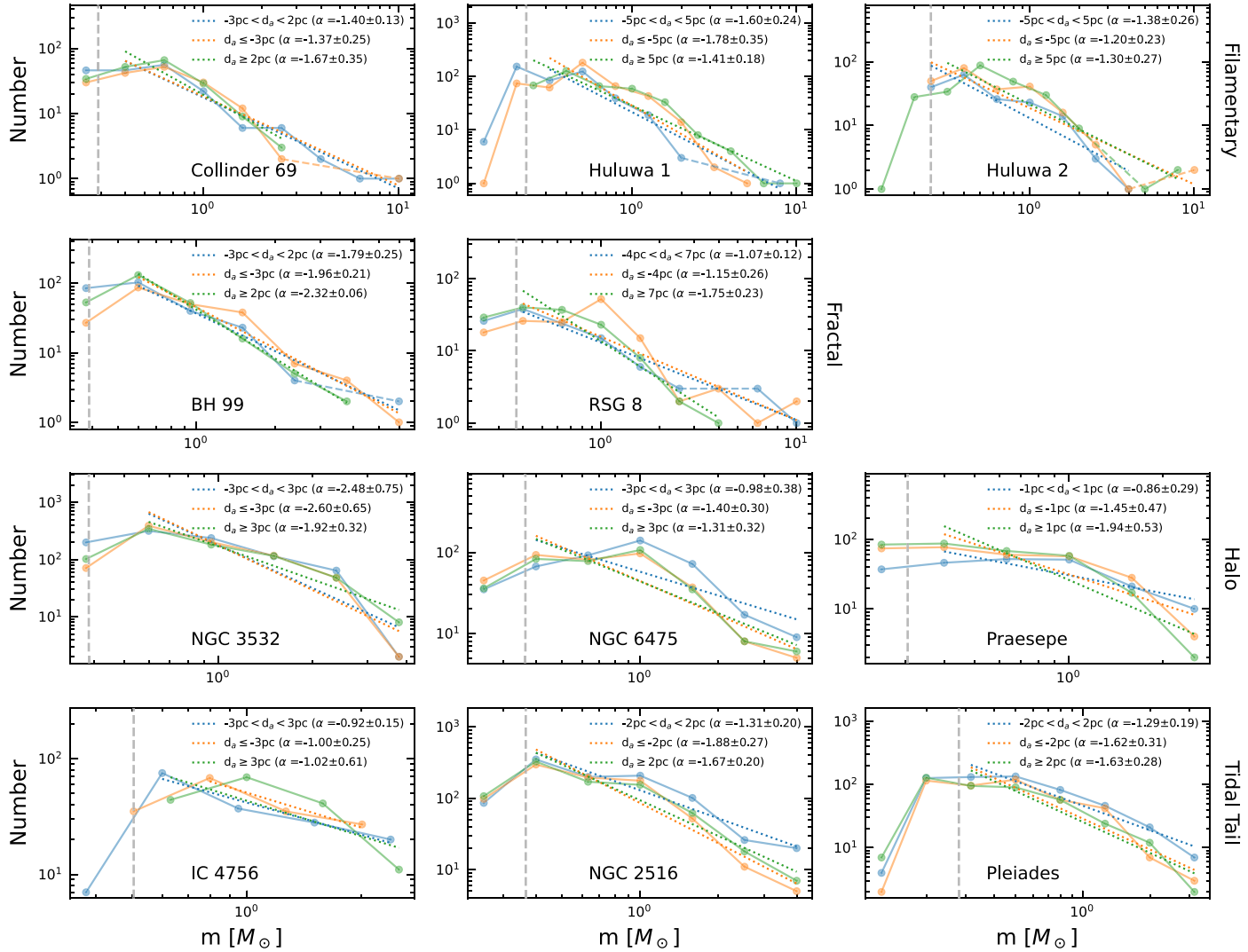

Figure 8. The stellar mass function for three regions along the semimajor axis d_a of the best-fitting ellipsoid of each representative cluster shown in Figure 6. The 3D position of each star is transformed into the coordinate system spanned by d_a, d_b, and d_c, which are the the semimajor, semimediate, and semiminor axes of the best-fitted ellipsoid from Pang et al. (2022b). The blue curve represents the mass function in the inner region, a few parsecs away from the center in the d_a direction. The orange and green curves are mass functions in the region on the left side (negative d_a values) and right side (positive d_a values) of the inner region along the d_a direction. The best fit to the mass function of each region is indicated with the dotted colored lines, whose slopes, α, and corresponding uncertainties are indicated in the upper right corner of each panel. The vertical gray dashed line is the Gaia completeness limit at the distance of the cluster.

the plane of the sky. The velocity of the photocenter of this unresolved binary only depends on the mass of the companion $qM_\odot$, the semimajor axis a, and the total G-band luminosity of the binary. Hence no assumption of distance is required.

For simplicity, the eccentricity of the binary system is assumed to be zero, and the barycenter of the system is assumed to have zero PM. We consider the astrometric observational baseline as 3 yr (Gaia Collaboration et al. 2022). A total of 36 random observing times are generated within this period of 3 yr. We compute the semimajor axis of the orbit of the photocenter using the mass of the companion. The mass–luminosity relation (Pecaut & Mamajek 2013) of MS stars is used in this step. The motion of the target system's photocenter in the orbital plane of the target system is fit with a linear model. The velocity of binary stars is converted into the Cartesian sky coordinate system using a rotational matrix, which is produced by the Gram–Schmidt process (Schmidt 1907). The matrix determines the orientation of the orbital plane and the initial phase of the velocity components. The velocity is projected onto the direction of the decl. The velocity difference of the photocenter and the barycenter is the bias triggered by binary systems. Since the barycenter is set to have zero PM, the magnitude of the projected value is the 1D tangential velocity bias from binary systems. This procedure is repeated 400 times to obtain the average bias for a given semimajor axis a distribution (Raghavan et al. 2010) and mass ratio q distribution (Fisher et al. 2005).

The results of the simulation are shown in Figure 10. For binary systems with longer periods (larger a), i.e., the right quadrant of Figure 10, the bias ΔV_t increases for smaller semimajor axes ($a < 100$ au) and larger companion masses ($q = 0.3$–0.9). However, short-period binary systems (the left quadrant in Figure 10 for $a < 1$ au) generally generate a smaller bias in the tangential velocity when the period becomes smaller. When $q = 1$, the barycenter of the binary system coincides with the photocenter, thus leading to zero bias for ΔV_t.

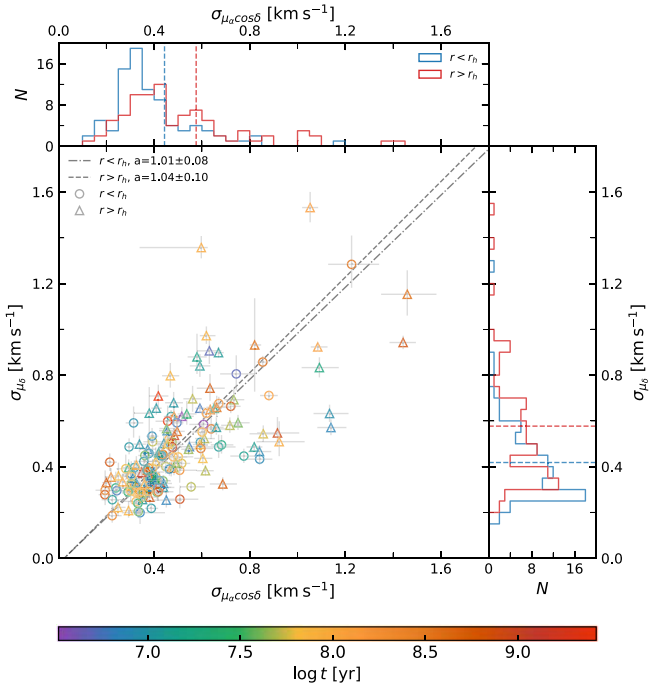

Figure 9. The distribution of the dispersion of the 1D tangential velocity, along the R.A. and decl. The velocity dispersion value is computed using the MCMC method (see Section 6). The circles indicate the dispersion values obtained from stars within the half-mass radius r_h and the triangles indicate stars outside r_h. The colors of the symbols are scaled with the cluster age (color bar). The dashed and dashed–dotted lines show the linear fits to the correlation of σ_{μ_α} and $\sigma_{\mu_\alpha \cos\delta}$ for the regions outside and inside r_h, respectively, with errors taken into consideration. The histograms in the upper and right panels represent the values of $\sigma_{\mu_\alpha \cos\delta}$ and σ_{μ_α} for the stars inside r_h (blue) and outside r_h (red). The blue and red dashed lines in the upper and right panels denote the mean values of $\sigma_{\mu_\alpha \cos\delta}$ and σ_{μ_α} for stars inside and outside r_h, respectively.

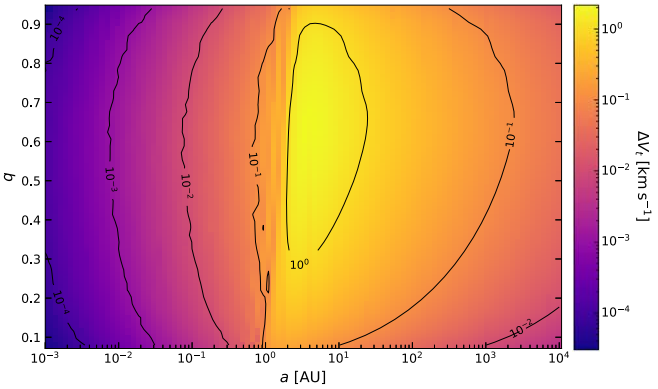

Figure 10. The dependence of the bias in the 1D tangential velocity along the decl. direction on the binary semimajor axis a and the mass ratio q. When calculating the bias, we assume a primary mass of 1 $M_\odot$. The color bar indicates the average 1D tangential velocity bias along the decl. direction.

Our identification approach recovers binaries with semimajor axis a less than 360 au (Section 3.3); accordingly, these kinds of unresolved binary systems induce an additional error that is 0.1–1 km s^{-1} (Figure 10) larger than that for the single stars in the measurement of the tangential velocity (obtained from the PM). We obtain the 1D tangential velocity dispersions of binary stars and single members, respectively, via the same MCMC method. The dispersion of the unresolved binary stars is 0.1–0.5 km s^{-1} larger than that for the single stars, as shown in Figure 9. However, this larger value might not be intrinsic. It could be caused by the bias induced by the unresolved binary systems. As shown in Figures 4–6, the unresolved binary fraction is higher at larger distances from the cluster center. Therefore, the unresolved binary fraction outside the half-mass radius is generally higher than that inside the half-mass radius. A higher velocity dispersion outside the half-mass radius is likely a consequence of the higher fraction of unresolved binary stars, which induce the larger uncertainty in the PM measurement. We propose this as one possibility for explaining the larger velocity dispersion outside the half-mass radius.

Therefore, based on the current accuracy of Gaia PM measurements, the higher dispersion of stars outside r_h (relative to those inside) might not be a pure dynamical signature. We are unable to draw a reliable conclusion about the internal kinematics of star clusters if the effects induced by the unresolved binaries are not properly considered and subtracted.

In the simulation described above, the binary population is not placed in a clustered environment, since our goal is not to investigate the dynamical evolution of binaries in star clusters. The latter would require N-body simulations, which is beyond the scope of our current study.

7. Crossmatch with Previous Works

Numerous investigations have been conducted to determine the binary fractions of star clusters using various methods. In this section, we compare the total binary fractions obtained in this work to those of previous studies and investigate the reasons for any discrepancies that may arise.

In the study by Jadhav et al. (2021), the binary fraction for $q > 0.6$ was estimated for 23 open clusters using a similar method via CMD. However, unlike the current study, they used a larger magnitude range of $M_G = 1$–10 mag in the Gaia absolute G magnitude to include a wider range of stars. We find that their binary fractions for all of the seven overlapped open clusters (IC 4756, NGC 2422, NGC 2516, NGC 2547, NGC 3532, NGC 6774, and the Pleiades) are consistent with the total binary fraction estimated in this study after completeness correction. Using infrared photometry, Malofeeva et al. (2022) identified binary candidates for the Pleiades cluster and estimated a binary fraction of 0.54 ± 0.11. In this study, a total binary fraction of 0.28–0.45 is derived for the Pleiades cluster, assuming different mass ratio distributions, which agrees with the value obtained in Malofeeva et al. (2022). The recent study of Malofeeva et al. (2023) updated the unresolved binary fraction for the Pleiades to 0.55 ± 0.02 and obtained a binary fraction of 0.45 ± 0.03 for Praesepe. Both values are higher than the binary fraction derived in this work.

30 clusters in our sample are also described in the study of Donada et al. (2023). The latter study also carried out distance-dependent completeness corrections for the binary fraction. In general, our results for the binary fraction (after completeness correction) are in agreement with their results, except for three clusters: Alessi 9, NGC 1901, and NGC 3228. For these clusters, we find higher binary fractions than Donada et al. (2023). This difference might be attributed to the different lower limit for the mass ratio ($q > 0.6$ in Donada et al. 2023) adopted when calculating the binary fraction.

Six clusters in our sample appear in the study of Cordoni et al. (2023), which obtained binary fractions for $q > 0.6$ using a similar method via the CMD as this work. All the binary fractions of the matched clusters (Pleiades, NGC 2442,

NGC 2516, NGC 2547, NGC 3532, and Stock 12) are consistent with our results within the uncertainties.

In the case of NGC 3532, Li et al. (2020) derived a binary fraction of 0.267, which agrees well with the total binary fraction estimated in this study assuming a uniform mass ratio distribution. Finally, Sollima et al. (2010) estimated binary fractions for five open clusters, ranging from 36% to 70%, with NGC 2516 overlapping with this study. In our study, we derive a total binary fraction of 27%–42% for NGC 2516, which is consistent with the binary fraction of $65.5\% \pm 24.3\%$ from Sollima et al. (2007).

The utilization of different methodologies to determine binary fractions yields both advantages and disadvantages. In compiling binary fractions for research purposes, it is imperative to consider the types of binaries that are being identified and the feasibility of the identification method, such as the range of the semimajor axis and the mass ratio, to ensure homogeneity in the resulting binary data.

8. Summary

Using the member catalogs from Pang et al. (2021a, 2021b, 2022b) and Li et al. (2021), we identify binary systems within 85 open clusters based on their locations in the CMD. Specifically, we select systems with mass ratios greater than $q_0 = 0.4$ as candidates. We define the binary region in the CMD as the region with an upper boundary at an absolute G magnitude (M_G) equal to 4 mag and a lower boundary at a stellar mass equal to 0.5 $M_\odot$ (see Section 3). The binary fraction, $f_{\rm bin}^{q>0.4}$, is computed as the number of binary systems relative to the total number of binary systems and single stars within each cluster.

The uncertainty of the binary fraction is estimated using Monte Carlo simulations. In this process, we generate artificial stars based on the photometric uncertainties and recompute the binary fraction using these simulated stars. We then compare this value to the observed binary fraction, $f_{\rm bin}^{q>0.4}$, and quantify the difference as the associated uncertainty.

To ensure an accurate measurement of the binary fraction, $f_{\rm bin}^{q>0.4}$, for each cluster, we adopt completeness correction to account for the limitation of Gaia's angular resolution of $0\farcs6$ at different distances. To achieve this, we estimate the completeness fraction $f_{\rm comp}$ using the lognormal semimajor axis distribution from Raghavan et al. (2010). The completeness-corrected binary fraction $f_{\rm binc}^{q>0.4}$ is then computed as the ratio of $f_{\rm bin}^{q>0.4}$ to $f_{\rm comp}$ within a given distance bin.

We consider three mass ratio distributions to extrapolate the $f_{\rm binc}^{q>0.4}$ to obtain the total binary fraction: Kouwenhoven et al. (2007 ;$f_{\rm k07}^{\rm tot}$), a uniform distribution ($f_{\rm uni}^{\rm tot}$), and Fisher et al. (2005 ;$f_{\rm f05}^{\rm tot}$). Below, we summarize our main findings regarding the binary candidates in the targeted clusters.

1. The relationship between the completeness-corrected binary fraction $f_{\rm binc}^{q>0.4}$ and cluster age exhibits a considerable dispersion across all age ranges. By excluding clusters or groups with $f_{\rm binc}^{q>0.4} > 0.4$, we observe a decreasing trend in the overall binary fraction with increasing cluster age.
2. The completeness-corrected binary fraction $f_{\rm binc}^{q>0.4}$ exhibits a positive correlation with cluster total mass for clusters with $M_{\rm cl} < 200\,M_\odot$. However, for clusters with $M_{\rm cl} > 200\,M_\odot$, $f_{\rm binc}^{q>0.4}$ appears to be independent of the cluster mass.
3. The local stellar density plays a crucial role in the dynamical binary evolution of binary systems. Our investigation has revealed a robust correlation between increasing stellar density within a cluster and a decrease in the binary fraction. We find this radial trend of binary fraction in various morphological types of clusters, which have different density environments. In the filamentary and fractal stellar groups, or clusters with the lowest density, we observe the highest binary fraction $f_{\rm binc}^{q>0.4}$, with mean values of $23.6\% \pm 9.2\%$ and $23.2\% \pm 7.2\%$, respectively. The tidal tail clusters exhibit a mean $f_{\rm binc}^{q>0.4}$ of approximately $20.8\% \pm 9.5\%$, while the densest halo-type clusters have the smallest binary fraction of $14.8\% \pm 9.5\%$.
4. We investigate the radial distribution of the binary fraction for representative clusters belonging to four distinct types. We find that the clusters of all four types showed a consistent trend, where the binary fraction is observed to be lowest within the half-mass radius ($r_{\rm h}$), and increases toward the larger clustercentric radius. This observation provides compelling evidence that the binary population experiences early disruption in the dense regions of clusters.
5. The analysis of a representative set of clusters belonging to four types of environments reveals a distinct pattern in the mean mass distribution. In particular, the filamentary groups exhibit inverse mass segregation, while the fractal-type clusters BH 99 and RSG 8, the halo-type cluster Praesepe, and the tidal tail cluster NGC 2516 display hints of mass segregation. However, considering the uncertainty, the observed mass segregation is not significant. Therefore, the observed mass segregation does not yet generate a global effect inside the target clusters. Furthermore, the tidal tail clusters and some expanding filamentary stellar groups were found to be in a disrupted state (Pang et al. 2022b), which was not conducive to the evolution of the binary population. Binary systems in such clusters are instead likely to follow the expanding flow and escape and are thus spared from internal dynamical processing.
6. By assuming a primary mass of 1 $M_\odot$, we estimate that the bias induced by unresolved binary systems in 1D tangential velocity along the decl. direction ranges from 0.1 to 1 km s^{-1}. Consequently, we cannot draw definitive conclusions regarding the internal kinematics of the clusters based on the present Gaia PM data.

Our study is limited by the angular resolution of the Gaia data. Moreover, the assumption of a primary mass of 1 $M_\odot$ in our simulation (Section 6) is a simplification made to estimate the bias in the 1D velocity dispersion induced by unresolved binary systems. Further studies using a wider range of primary masses are needed to address these limitations. Our findings demonstrate that it is worthwhile continuing investigations of the relationship between the binary fraction and environmental properties, such as the cluster age, mass, and stellar density, with higher-resolution data. Future spectroscopic and astrometric data from space-based and ground-based telescopes will provide a better understanding of the formation and evolution of binary systems in open clusters.

Acknowledgments

We thank the anonymous referee for providing helpful comments and suggestions that helped to improve this paper. We thank Yuqian Li for help with the ellipsoid coordinate transformation, Danchen Wang for help with the velocity dispersion computation, and Teng Zhang for constructive discussions. Xiaoying Pang acknowledges financial support from the National Natural Science Foundation of China through grants 12173029 and 12233013, the Natural Science Foundation of Jiangsu Province (No. BK20200252), and the research development fund of Xi'an Jiaotong-Liverpool University (RDF-18–02–32). M.B.N.K. acknowledges support from the National Natural Science Foundation of China (grant 11573004) and Xi'an Jiaotong-Liverpool University (grant RDF-SP-93).

This work has made use of data from the European Space Agency (ESA) mission Gaia (https://www.cosmos.esa.int/gaia), processed by the Gaia Data Processing and Analysis Consortium (DPAC, https://www.cosmos.esa.int/web/gaia/dpac/consortium). This study also made use of the SIMBAD database and the VizieR catalog access tool, both operated at CDS, Strasbourg, France.

Software: `Astropy` (Astropy Collaboration et al. 2013, 2018, 2022), `SciPy` (Millman & Aivazis 2011), `TOPCAT` (Taylor 2005), and STARGO (Yuan et al. 2018).

ORCID iDs

Xiaoying Pang https://orcid.org/0000-0003-3389-2263
Yifan Wang https://orcid.org/0000-0002-7117-9533
Shih-Yun Tang https://orcid.org/0000-0003-4247-1401
Yicheng Rui https://orcid.org/0000-0001-5295-1682
Fabo Feng https://orcid.org/0000-0001-6039-0555
M. B. N. Kouwenhoven https://orcid.org/0000-0002-1805-0570
Wen-Ping Chen https://orcid.org/0000-0003-0262-272X
Rwei-ju Chuang https://orcid.org/0000-0001-6355-0673

References

Allison, R. J., Goodwin, S. P., Parker, R. J., et al. 2009, ApJL, 700, L99
Astropy Collaboration, Price-Whelan, A. M., Lim, P. L., et al. 2022, ApJ, 935, 167
Astropy Collaboration, Price-Whelan, A. M., Sipőcz, B. M., et al. 2018, AJ, 156, 123
Astropy Collaboration, Robitaille, T. P., Tollerud, E. J., et al. 2013, A&A, 558, A33
Bailer-Jones, C. A. L. 2015, PASP, 127, 994
Baraffe, I., Homeier, D., Allard, F., & Chabrier, G. 2015, A&A, 577, A42
Bate, M. R. 2012, MNRAS, 419, 3115
Bressan, A., Marigo, P., Girardi, L., et al. 2012, MNRAS, 427, 127
Carrera, R., Pasquato, M., Vallenari, A., et al. 2019, A&A, 627, A119
Chen, Y., Bressan, A., Girardi, L., et al. 2015, MNRAS, 452, 1068
Cohen, R. E., Geller, A. M., & Hippel, T. v. 2019, AJ, 159, 11
Cordoni, G., Milone, A. P., Marino, A. F., et al. 2018, ApJ, 869, 139
Cordoni, G., Milone, A. P., Marino, A. F., et al. 2023, A&A, 672, A29
de Grijs, R., Li, C., Zheng, Y., et al. 2013, ApJ, 765, 4
Deacon, N. R., & Kraus, A. L. 2020, MNRAS, 496, 5176
Dinnbier, F., & Kroupa, P. 2020, A&A, 640, A84
Donada, J., Anders, F., Jordi, C., et al. 2023, A&A, 675, A89
Duchêne, G., & Kraus, A. 2013, ARA&A, 51, 269
Fisher, J., Schröder, K.-P., & Smith, R. C. 2005, MNRAS, 361, 495
Gaia Collaboration, Brown, A. G. A., Vallenari, A., et al. 2021, A&A, 649, A1
Gaia Collaboration, Vallenari, A., Brown, A., et al. 2022, A&A, 674, A1
Geller, A. M., de Grijs, R., Li, C., & Hurley, J. R. 2013, ApJ, 779, 30
Geller, A. M., Grijs, R. d., Li, C., & Hurley, J. R. 2015, ApJ, 805, 11
He, C., Sun, W., Li, C., et al. 2022, ApJ, 938, 42
Heggie, D., & Hut, P. 2003, The Gravitational Million-Body Problem: A Multidisciplinary Approach to Star Cluster Dynamics (Cambridge: Cambridge Univ. Press)
Herczeg, G. J., & Hillenbrand, L. A. 2014, ApJ, 786, 97
Hurley, J. R., Tout, C. A., Aarseth, S. J., & Pols, O. R. 2001, MNRAS, 323, 630
Jadhav, V. V., Roy, K., Joshi, N., & Subramaniam, A. 2021, AJ, 162, 264
Jaehnig, K., Bird, J. C., Stassun, K. G., et al. 2017, ApJ, 851, 14
Jerabkova, T., Beccari, G., Boffin, H. M. J., et al. 2019, A&A, 627, A57
Kounkel, M., Covey, K., Moe, M., et al. 2019, AJ, 157, 196
Kouwenhoven, M. B. N. 2006, PhD thesis, University of Amsterdam
Kouwenhoven, M. B. N., Brown, A. G. A., Goodwin, S. P., Portegies Zwart, S. F., & Kaper, L. 2009, A&A, 493, 979
Kouwenhoven, M. B. N., Brown, A. G. A., Portegies Zwart, S. F., & Kaper, L. 2007, A&A, 474, 77
Kouwenhoven, M. B. N., Brown, A. G. A., Zinnecker, H., Kaper, L., & Portegies Zwart, S. F. 2005, A&A, 430, 137
Kraus, A. L., Ireland, M. J., Martinache, F., & Hillenbrand, L. A. 2011, ApJ, 731, 8
Kroupa, P. 2001, MNRAS, 322, 231
Kruijssen, J. M. D. 2012, MNRAS, 426, 3008
Li, C., de Grijs, R., & Deng, L. 2013, MNRAS, 436, 1497
Li, C., de Grijs, R., Deng, L., & Milone, A. P. 2017, ApJ, 844, 119
Li, C., Sun, W., Grijs, R. d., et al. 2019, ApJ, 876, 65
Li, L., Shao, Z., Li, Z.-Z., et al. 2020, ApJ, 901, 49
Li, Y., Pang, X., & Tang, S.-Y. 2021, RNAAS, 5, 173
Lindegren, L., Klioner, S. A., Hernández, J., et al. 2021, A&A, 649, A2
Lodieu, N., Pérez-Garrido, A., Smart, R. L., & Silvotti, R. 2019, A&A, 628, A66
López-Valdivia, R., Sokal, K. R., Mace, G. N., et al. 2021, ApJ, 921, 53
Malofeeva, A. A., Mikhnevich, V. O., Carraro, G., & Seleznev, A. F. 2023, AJ, 165, 45
Malofeeva, A. A., Seleznev, A. F., & Carraro, G. 2022, AJ, 163, 113
Millman, K. J., & Aivazis, M. 2011, CSE, 13, 9
Milone, A. P., Piotto, G., Bedin, L. R., & Sarajedini, A. 2008, MmSAI, 79, 623
Milone, A. P., Piotto, G., Bedin, L. R., et al. 2012, A&A, 540, A16
Moe, M., Kratter, K. M., & Badenes, C. 2019, ApJ, 875, 61
Moeckel, N., & Bally, J. 2007, ApJL, 661, L183
Niu, H., Wang, J., & Fu, J. 2020, ApJ, 903, 93
Offner, S. S. R., Moe, M., Kratter, K. M., et al. 2022, arXiv:2203.10066
Pang, X., Grebel, E. K., Allison, R. J., et al. 2013, ApJ, 764, 73
Pang, X., Li, Y., Tang, S.-Y., Pasquato, M., & Kouwenhoven, M. B. N. 2020, ApJL, 900, L4
Pang, X., Li, Y., Yu, Z., et al. 2021a, ApJ, 912, 162
Pang, X., Shen, S., & Shao, Z. 2018, ApJL, 868, L9
Pang, X., Shu, Q., Wang, L., & Kouwenhoven, M. B. N. 2022a, RAA, 22, 095015
Pang, X., Tang, S.-Y., Li, Y., et al. 2022b, ApJ, 931, 156
Pang, X., Yu, Z., Tang, S.-Y., et al. 2021b, ApJ, 923, 20
Parker, R. J., & Goodwin, S. P. 2012, MNRAS, 424, 272
Parker, R. J., Goodwin, S. P., & Allison, R. J. 2011, MNRAS, 418, 2565
Parker, R. J., Goodwin, S. P., Kroupa, P., & Kouwenhoven, M. B. N. 2009, MNRAS, 397, 1577
Parker, R. J., & Meyer, M. R. 2014, MNRAS, 442, 3722
Pecaut, M. J., & Mamajek, E. E. 2013, ApJS, 208, 9
Portegies Zwart, S. F., Hut, P., McMillan, S. L. W., & Makino, J. 2004, MNRAS, 351, 473
Portegies Zwart, S. F., McMillan, S. L. W., Hut, P., & Makino, J. 2001, MNRAS, 321, 199
Raghavan, D., McAlister, H. A., Henry, T. J., et al. 2010, ApJS, 190, 1
Reipurth, B., Clarke, C. J., Boss, A. P., et al. 2014, arXiv:1403.1907
Reipurth, B., Guimarães, M. M., Connelley, M. S., & Bally, J. 2007, AJ, 134, 2272
Riello, M., De Angeli, F., Evans, D. W., et al. 2021, A&A, 649, A3
Röser, S., & Schilbach, E. 2019, A&A, 627, A4
Sana, H., de Mink, S. E., de Koter, A., et al. 2012, Sci, 337, 444
Schmidt, E. 1907, MatAn, 63, 433
Shu, Q., Pang, X., Flammini Dotti, F., et al. 2021, ApJS, 253, 14
Sollima, A., Beccari, G., Ferraro, F. R., Fusi Pecci, F., & Sarajedini, A. 2007, MNRAS, 380, 781
Sollima, A., Carballo-Bello, J. A., Beccari, G., et al. 2010, MNRAS, 401, 577
Taylor, M. B. 2005, in ASP Conf. Ser. 347, Astronomical Data Analysis Software and Systems XIV, ed. P. Shopbell, M. Britton, & R. Ebert (San Francisco, CA: ASP), 29
Torniamenti, S., Pasquato, M., Di Cintio, P., et al. 2022, MNRAS, 510, 2097
Torres, G., Latham, D. W., & Quinn, S. N. 2021, ApJ, 921, 117
Wang, Y., Liao, S., Giacobbo, N., et al. 2022, A&A, 665, A111
Ye, X., Zhao, J., Zhang, J., Yang, Y., & Zhao, G. 2021, AJ, 162, 171
Yuan, Z., Chang, J., Banerjee, P., et al. 2018, ApJ, 863, 26